Origin of the Oligocene Tuolangla porphyry–skarn Cu–W–Mo deposit in Lhasa terrane, southern Tibet

Yong Huang, Ming–hua Ren, Wei Liang, Guang–ming Li, Kelly Heilbronn, Zuo–wen Dai, Yi–yun Wang, Li Zhang

Citation: Yong Huang, Ming–hua Ren, Wei Liang, Guang–ming Li, Kelly Heilbronn, Zuo–wen Dai, Yi–yun Wang, Li Zhang, 2020. Origin of the Oligocene Tuolangla porphyry–skarn Cu–W–Mo deposit in Lhasa terrane, southern Tibet, China Geology, 3, 369–384. doi: 10.31035/cg2020047.

View online: https://doi.org/10.31035/cg2020047

Related articles that may interest you

Zircon U–Pb age, trace element and Hf isotope composition of Sepon Au–Cu deposit, Laos: tectonic and metallogenic implications
China Geology. 2018, 1(1), 36 https://doi.org/10.31035/cg2018006

Zircon U–Pb ages of the two–periods magmatism from the Xiuwacu Mo–W–Cu deposit, northwest Yunnan, China
China Geology. 2019, 2(3), 391 https://doi.org/10.31035/cg2018110

Re–Os age report of pyrrhotite in the Dhi Samir amprophyre–type copper–nickel sulfide deposit in Yemen
China Geology. 2019, 2(2), 238 https://doi.org/10.31035/cg2018107

Baddeleyite and zircon U–Pb ages of the ultramafic rocks in Chigu Tso area, Southeastern Tibet and their constraints on the timing of Comei Large Igneous Province
China Geology. 2020, 3(2), 262 https://doi.org/10.31035/cg2020017

Multiphase porphyry intrusions in the Sungun copper deposit, NW Iran: Evidence from SHRIMP zircon U–Pb dating
China Geology. 2019, 2(2), 240 https://doi.org/10.31035/cg2018102

Zircon SHRIMP U–Pb dating of the Neogene coral reefs, Xisha Islands, South China Sea: implications for tectonic evolution
China Geology. 2018, 1(1), 49 https://doi.org/10.31035/cg2018007

China Geology 3 (2020) 369−384

China Geology

Journal homepage: http://chinageology.cgs.cn
https://www.sciencedirect.com/journal/china-geology

Origin of the Oligocene Tuolangla porphyry-skarn Cu-W-Mo deposit in Lhasa terrane, southern Tibet

Yong Huang[a, b,*], Ming-hua Ren[b], Wei Liang[a], Guang-ming Li[a], Kelly Heilbronn[c], Zuo-wen Dai[a, d], Yi-yun Wang[a], Li Zhang[a]

[a] *Chengdu Center, China Geological Survey, Ministry of Natural Resources, Chengdu* 610081, *China*
[b] *Department of Geoscience, University of Nevada, Las Vegas, NV* 89154-4010, *USA*
[c] *Economic Geology Research Center, James Cook University, Townsville* 4811, *Australia*
[d] *College of Earth Sciences, Chengdu University of Technology, Chengdu* 610059, *China*

ARTICLE INFO

Article history:
Received 15 April 2020
Received in revised form 1 June 2020
Accepted 5 June 2020
Available online 7 August 2020

Keywords:
Porphyry skarn type Cu-W-Mo deposit
Geochronology
Re-Os isotopic age
Zircon U-Pb isotopic age
Tuolangla
Gangdese belt
Tibet
China

ABSTRACT

Although some porphyry-skarn deposits occur in post-collisional extensional settings, the post-collisional deposits remain poorly understood. Here the authors describe the igneous geology, and mineralization history of Tuolangla, a newly-discovered porphyry-skarn Cu-W-Mo deposit in southern Tibet that belongs to the post-collisional class. The deposit is associated with Lower Cretaceous Bima Formation. It was intruded by granodiorite porphyry intrusions at about 23.1 Ma. Field investigation indicated that mineralization is spatially and temporally associated with granodiorite porphyry. Molybdenite yielded a Re-Os weighted mean age of 23.5 ± 0.3 Ma and is considered to represent the age of skarn mineralization at the deposit. The $\delta^{34}S$ values of sulfides, concentrated in a range between 0.6‰ to 3.4‰, show that the sulfur has a homogeneous source with characteristics of magmatic sulfur. The Pb isotopic compositions of sulfides indicate that ore-forming metal materials were derived from the mantle and ancient crust. The granodiorite porphyry displays high SiO_2 (68.78%–69.75%) and K_2O (3.40%–3.56%) contents, and relatively lower Cr (2.4×10^{-6}–4.09×10^{-6}), Ni (2.79×10^{-6}–3.58×10^{-6}) contents, and positive $\varepsilon_{Hf}(t)$ values (7.7–12.9) indicating that the mineralization porphyry was derived from the partial melting of juvenile lower crust. The Tuolangla deposit is located in the central part of Zedang terrane. This terrane was once considered an ancient terrane. This terrane is in tectonic contact with Cretaceous ophiolitic rocks to its south and Mesozoic continental margin arc volcanics and intrusions of the Gangdese batholith of the Lhasa terrane to its north. Thus, the authors proposed that the Oligocene porphyry skarn Cu-W-Mo mineralization is probably associated with the Zedang terrane. This finding may clarify why the Oligocene (about 23 Ma) deposits are found only in the Zedang area and why mineralization types of the Oligocene mineralization are considerably different from those of the Miocene (17–14 Ma) mineralization.

©2020 China Geology Editorial Office.

1. Introduction

Porphyry copper deposits provide the largest source of copper and molybdenum, and are an important resource of tungsten and gold in the world. Porphyry copper systems are generally located in island and continental arc settings in association with subduction-related magma and usually include porphyry deposits, skarn, carbonate-replacement, and high- and intermediate- sulfidation epithermal deposits (Sillitoe RH, 2010). However, continent-continent collisional orogenic belts can also be a major tectonic driver for the formation of porphyry copper systems, such as in the Gangdese porphyry copper belt and Yulong belt of Tibet (Hou ZQ et al., 2009a, 2011, 2015; Qu XM et al., 2007; Yang ZM et al., 2009). In the past 20 years, a lot of prospecting and exploration has been carried out in south Tibet resulting in the discovery of a large group of porphyry copper and skarn Pb-Zn-Ag, Cu-Mo±Au, Cu-W-Mo deposits in the southern margin of Tibet (Gangdese metallogenic belt) (Hou ZQ et al., 2015; Qu XM et al., 2007; Huang Y et al., 2013). The belt extends along the northern side of Yarlung Tsangpo River with an EW-strike, parallel to the Indian-Asian continent-continent collisional belt (Qu XM et al., 2007). Ongoing

* Corresponding author: *E-mail address*: 327016045@qq.com (Yong Huang).

doi:10.31035/cg2020047
2096-5192/© 2020 China Geology Editorial Office.

exploration and preliminary evaluations indicate that the Gangdese metallogenic belt is a giant porphyry copper belt, with total resources of >35 ×10^6 t Cu (Beaudoin G et al., 2005; Hou ZQ et al., 2015; Li JX et al., 2011). Recent studies indicate that the Gangdese metallogenic belt is a significant but poorly understood setting (Hou ZQ et al., 2009a, 2015; Hou ZQ and Cook NJ, 2009b; Tafti R et al., 2014;Yang ZM et al., 2016; Yang YF et al., 2019). Previous studies mainly focus on the Miocene magmatic rocks and its related porphyry copper deposits. The petrogenesis of ore-forming intrusions and ore controls, such as magma and metal source, magmatic oxidation state, geodynamic setting, of the Miocene porphyry deposits in Gangdese metallogenic belt have been widely studied (Yang ZM et al., 2016; Hou ZQ et al., 2004, 2009a, 2012, 2015, 2017; Huang Y et al., 2017, Qu XM et al., 2007; Meng XJ et al., 2003; Rui ZY et al., 2003). By contrast, the metallogenesis and ore controls of Oligocene porphyry-skarn deposits in Gangdese metallogenic belt are still unclear although a few studies have focused on the petrogenesis of ore-related intrusions, fluid inclusions, ore-related source of individual deposits (Chen L et al., 2015; Li GM et al., 2006).

The Oligocene mineralization mainly occurred in the Zedang area where several vital porphyry-skarn deposits are located including two porphyry-skarn Cu-W-Mo deposits (Nuri and Tuolangla), four porphyry Mo±Cu deposits (Mingze, Chengba, Panan, and Chumuda) (Figs. 1a, b). The molybdenite Re–Os dating on these deposits defined an age range of 30 Ma to 23 Ma (Li GM et al., 2006; Chen L et al., 2015; Duan LF et al., 2014; Wu CD et al. 2015; Zhang S et al., 2012; Sun X et al., 2013; Zheng YY et al., 2015). Whereas, the ore-forming intrusions associated with these deposits and metal resources are still unclear. Some researches documented that Early Oligocene granodiorite and granite porphyry (33 Ma to 30 Ma) are related to all of these deposits. These Oligocene intrusions have similar geochemical signatures, such as relatively low $^{87}Sr/^{86}Sr$ ratios (0.7061 to 0.7066), low $\varepsilon_{Nd}(t)$ (−3.8 to −1.8), high Sr/Y ratios, and variable $\varepsilon_{Hf}(t)$ values (+0.6 to +10.1) (Chen L et al., 2015; Zheng YY et al., 2015; Sun X et al., 2013), exhibiting the arc magmatic affinities. However, these stocks are apparently older than Cu-W-Mo mineralization ages (Tuolangla: 23.51 ± 0.29 Ma; Nuri: 23.36 ± 0.49 Ma).

In this study, the authors present detailed geological observations, whole rock geochemistry, zircon U-Pb and molybdenite Re-Os ages, sulphide S, Pb isotopes and Hf isotopic data for Oligocene intrusive associated with the Tuolangla Cu-W-Mo deposit. The authors will confine the timing of mineralization, geochemically ascertain the magma sources and petrogenesis of the intrusives and discuss the tectonic model for Oligocene Cu-W-Mo metallogenic events within GPCB.

2. Geological background

2.1. Regional Geology

The Tibetan plateau is a product of collision of the Asian plate with the Indian plate (Beaudoin G et al., 2005). From south to north, Tibet consists of the Himalaya, Lhasa, Qiangtang, Songpan-Ganze, and Kunlun-Qaidam terranes (Yin A and Harrison TM, 2000; Wang YY et al., 2020; Tang Y et al., 2020).

The Lhasa terrane (Zhu DC et al., 2011), also named the Gangdese orogenic belt (Pan GT et al., 2006) or Lhasa block (Yin A et al., 2010), is bounded by the Indus-Yarlung Tsangpo suture (IYTS) to the south and the Banggong-Nujiang suture (BNS) to the north (Yin A and Harrison TM, 2000). The Lhasa terrane is composed of Mid-Proterozoic and Early Cambrian basement and Paleozoic to Mesozoic cover strata including a sequence of Ordovician to Triassic shallow marine clastic sedimentary rocks (Burg JP and Chen GM, 1984). As an important part of Tibetan Plateau collision orogenic system, the Lhasa terrane recorded Tethys ocean subduction, convergence, and collision history (Hou ZQ et al., 2011, 2013; Meng YK et al., 2018) and formed a giant metallogenic belt. The terrane is divided into the northern Gangdese, central Gangdese, Gangdese back-arc fault uplift belt, and southern Gangdese, separated by the Shiquan River-Nam Tso Mélange Zone, Gar-Lunggar-Zhari Nam Tso-Comai Fault and Shamolei-Maila-Luobadui-Milashan Fault, respectively (Zhu DC et al., 2011). The Lhasa terrane underwent early subduction and subsequent collision, and therefore can be regarded as a suitable region for investigating the metallogeneisis related to accretionary orogenesis and collisional orogenesis. Recently, numerous collision-related deposits have been explored (Hou ZQ et al., 2009a, 2015; Sun X et al., 2017; Zheng YY et al., 2015). The collision-related deposits have been divided into eight principle types: (1) Porphyry Cu-Mo, (2) orogenic Au, (3) granite-related Sn-W-U, (4) alkali complex-related REE, (5) sediment-hosted Zn-Pb(-Cu-Ag), (6) vein-type Sb-Au, (7) skarn polymetallic, and (8) hot spring-type Cs-Au deposits.

Mesozoic magmatism, ranging from 180 Ma to 70 Ma, along the southern margin of the Lhasa Terrane forms a narrow arc-type mountain belt. Arc-related Cu-Au porphyry mineralization was formed at this stage, such as Xiongcun porphyry Cu-Au deposit (Tafti R et al., 2009; Tang JX et al., 2015). Later Cenozoic magmatism, 64.5 Ma to 44 Ma, in south Tibet formed the Cenozoic Linzizong volcanic succession, the Paleocene syn-collisional peraluminous granites, and grabbro bodies (Lee HY et al., 2009; Mo XX et al., 2008; Zhou S et al., 2004). The porphyry Mo deposits were formed at this stage, such as Sharang porphyry Mo deposit (Zhao JX et al., 2015; Zhao JX et al., 2014). The Miocene magmatism of the Lhasa Terrane formed a Miocene potassic igneous belt, extending for about 1500 km and intruded the Gangdese granitoid batholiths and surrounding Triassic to Cenozoic sedimentary sequence as intrusions. This potassic igneous belt mainly consists of potassic calc-alkaline lavas, ultra-potassic lavas (Miller C et al., 1999; Turner S et al., 1996), and potassic Cu-bearing porphyry intrusions which mainly derived from partial melting of juvenile lower crust (Hou ZQ et al., 2009). The age of Cu-bearing porphyry intrusion has been constrained by Zircon U-Pb. These ages range from 30 Ma to 13.3 Ma, peaking at 15 Ma (Hou ZQ et al., 2009a; Wang LL et al., 2006). The mineralization types of these deposits are porphyry and/or skarn Cu-Mo±Au, Cu-Pb-

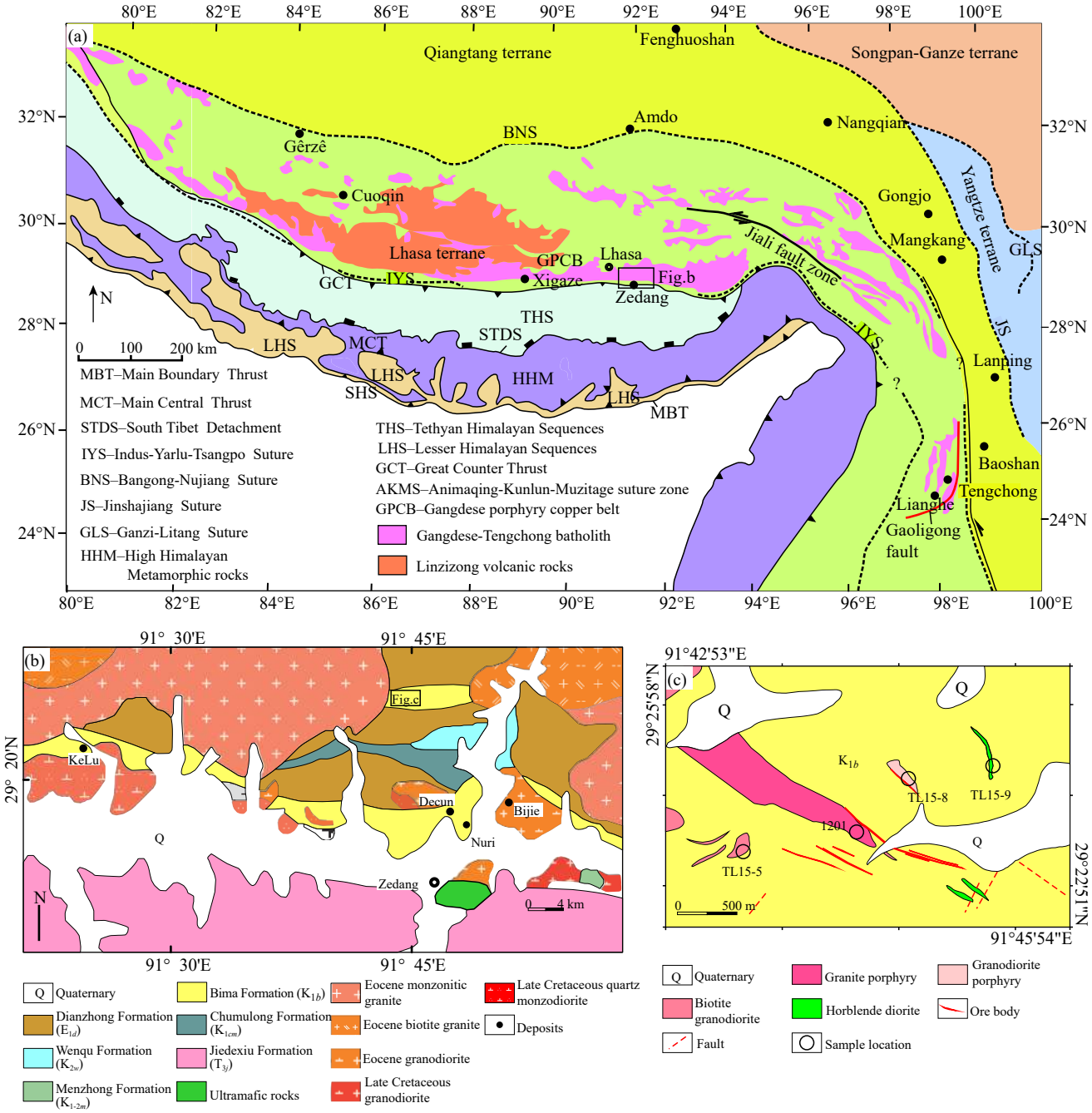

Fig. 1. a–Map of regional geology (modified from Yin A and Harrison TM, 2000); b–distribution of ore deposits in the Shannan area, south-eastern Gangdese (modified from Chung et al., 2009; Jiang ZQ et al., 2011); c–geologic sketch map of the Tuolangla Cu-W-Mo deposit.

Zn-Ag, Cu-W-Mo (Huang Y et al., 2017; Li GM et al., 2005; Meng XJ et al., 2003; Rui ZY et al., 2003; Ying LJ et al., 2010, 2014; Li GM et al., 2006; Wu CD et al,. 2015; Zhang S et al., 2012).

Strata in the Zedang district is dominated by a Jurassic to Cretaceous marine sedimentary sequence with volcanic rocks (Fig. 1b). The Upper Jurassic Jiedexiu Formation is mainly distributed in the south part the Zedang district and consists of marine siltite and slate. Early Cretaceous strata, including the Wenqu Formaion, Menzhong Formation, Chumulong Formation, and Bima Formation, formed as the product of the northward subduction of the Neo-tethys ocean (Fig. 1b). These formations are comprised of sandstone, siltite, slate and limestone, and minor volcanic rocks. The Bima Formation consists of limestone and minor marble which are the important host rocks for mineralization in the Zedang district (Fig. 1c) (Chen L et al., 2015). The Eocene Dianzhong Formation, consisting of mafic to felsic volcanic rocks, is the main rocks outcropping in the Zedang district that formed as the product of collision between Indian and Asian continents (Mo XX et al., 2007, 2008; Lee HY et al., 2009).

2.2. Geological background of ore field

The Tuolangla deposit is located northwest of the Nuri

deposit (Figs. 1b, c). Two main lithologic units have been developed in the district: (1) the Lower Cretaceous Bima Formation, which are mainly composed of limestone and marble, and (2) Mesozoic to Miocene intrusions with outcrop area of 3 km^2, mainly consisting of medium, medium-acid to acid granites, including granite porphyry, biotite granodiorite, hornblende diorite, and granodiorite porphyry. The dominant mineralization phase is linked to the Oligocene granodiorite porphyry with a zircon U-Pb age of 23.08 Ma, which intruded Lower Cretaceous Bima Formation. At the outer contact zone between intrusions and sedimentary strata, hydrothermal metasomatic alteration, skarn, metal mineralization formed.

There are two main groups of faults in the ore district: Northwest strike and northeast strike. The northwest strike faults with northeast dipping direction are 1.5 km to 2 km long, and controls the distributions of skarn zone and main ore orebodies (Fig. 1c).

2.2.1. Intrusions

The main igneous units present at Tuolangla include Late Cretaceous granite porphyry, Paleocene biotite granodiorite, hornblende diorite dykes, and ore-related Oligocene granodiorite porphyry. Features of these intrusions are presented below.

The granite porphyry is the largest intrusion at Tuolangla with an outcrop area of about 0.7 km^2 (Fig. 1c). This porphyry trends northwest, is approximately 1.6 km in length, and has variable width of 0.2–0.6 km. Phenocrysts range from 30% to 40% total volume, are relatively large, and include K-feldspar (0.3–2 cm), plagioclase (0.5–1.5 cm), and quartz (0.3–1.2 cm) (Figs. 2a, b). The groundmass of the granite porphyry is quartz-feldspathic and consists of fine-grained plagioclase, K-feldspar, quartz, and biotite. Accessory minerals include apatite, rutile and zircon. Emplacement of this porphyry stock caused weak contact metasomatism of the surrounding Bima formation, forming a weak skarn mineral association. The granite porphyry has experienced weak to moderate phyllic and argillic alteration.

The biotite granodiorite is exposed in the east part of the deposit and is characterized by a medium-grained granitic texture and is gray in color. The outcrop area of the biotite granodiorite is less than 0.4 km^2 (Fig. 1c). It consists of plagioclase, quartz, K-feldspar, biotite and minor hornblende. Accessory minerals include apatite and zircon (Figs. 2c, d). The biotite granodiorite is relatively fresh, and some weak argillization.

The hornblende diorite occurs as dikes at the Tuolangla deposit. Individual dikes are generally 2 –5 m wide and intrude the Bima Formation. The dikes consist of plagioclase, hornblende, biotite and minor quartz (Figs. 2e, f). The hornblende diorite is relatively fresh with weak phyllic alteration. A few small, disseminated pyrite grains and pyrite veinlets have also been identified in the hornblende diorite.

The granodiorite porphyry is characterized by a fine-grained porphyritic texture. It is exposed in the center of the deposit with an outcrop area less than 0.4 km^2 (Fig. 1c). In general, phenocryst phases that are within the porphyry range in abundance from 20% –40% total volume, are relatively small and include K-feldspar (0.2 –0.4 cm), plagioclase (0.3 –0.8 cm), and quartz (0.5 –1.2 cm) (Figs. 2g, h). The groundmass of the granodiorite porphyry consists of fine-grained plagioclase, k-feldspar, quartz, and biotite. Accessory minerals include apatite, zircon. The granodiorite porphyry is characterized by veinlet-disseminated chalcopyrite, pyrite and molybdenite mineralization and has potassic and phyllic alteration which further indicate that the mineralization is spatially related to granodiorite porphyry.

2.2.2. Mineralization

Porphyry-skarn mineralization at the Tuolangla Cu-W-Mo deposit is spatially and temporally related to the granodiorite porphyry. Several drill holes extend over a vertical interval of 548 m. Ten ore-bodies, including copper ore, tungsten ore, and copper-molybdenum-tungsten complex ore-bodies, were identified at Tuolangla. The ore-bodies have an overall strike of 110° –124° and trend to the southwest. The dip angle is 65°–83°. Several vein types are present in the drill core which include, listing from oldest to youngest, Quartz-magnetite-sulfide vein (Figs. 3a, b), quartz-sulfide vein (chalcopyrite-pyrite) (Figs. 3c, d), quartz-molybdenite (Figs. 3e, g), pyrite-quartz vein (Fig. 3h), quartz-sulfide-epidote vein (Fig. 3i), and barrenly white quartz vein (Fig. 3f). These veins crosscut the surrounding wall rocks, skarn and pre-mineralization granite porphyry. The skarn minerals include garnet, pyroxene, wollastonite, epidote, and actinolite. Garnets accounting for 50% –60% of the total skarn minerals are usually brown to red-brown. The diameter of garnets are generally less than 5 mm. Apparently zoned garnets are observed on a microscopic scale. Diopside usually replaced by epidote is another important skarn mineral. Wollastonite is usually distributed in particle gaps in garnet and/or diopside.

Ore minerals include chalcopyrite, scheelite, molybdenite. Chalcopyrite occurs as disseminated grains and in vein or veinlets, accompanied by magnetite or fine-grained pyrite and molybdenite (Figs. 4a, d). Molybdenite mainly occurs in veinlets accompanies by quartz and chalcopyrite. Scheelite grains are found within skarn and is accompanied by chalcopyrite and pyrite (Figs. 4e, f). Based on the interspersed relationship of veins, ore texture and mineral composition, the mineralizaton of the Tuolangla deposit can be divided into skarn stage, retrograde stage, and supergene oxidation stage. Andydrous silicate, such as, garnet, wollastonite, formed in the skarn stage. Scheelite formed in the early period of the retrograde stage. Sulfides (such as chalcopyrite, molybdenite, pyrite) are mainly present in the retrograde stage.

3. Sampling and analytical methods

Zircon U-Pb LA-ICPMS dating, Hf isotope analyses were performed on samples of granodiorite porphyry, hornblende diorite, and granite porphyry. Granodiorite porphyries were selected from the center part of the deposit (Sample TL15-8, 29°24.969′N, 91°45.728′E), and hornblende diorites sample from the northeast part of the deposit (Sample TL15-9,

29°24.278′N, 91°44.746′E). The granite porphyry sample was taken from drill hole ZK1201 (Sample 1201, 144.5 m in depth). Twenty-five sulfides (chalcopyrite, pyrite, and molybdenite) were selected for S, Pb isotopic analysis and Re-Os dating. Three samples of the ore-related granodiorite porphyry were selected for petrographic, whole-rock geochemical analyses. Detailed experimental procedures are presented in Appendix A. The results of zircon analysis are listed in Table 1. Whole-rock major, trace element and Re-Os aging data are presented in Supplementary Tables S1, and Table 2, respectively. S and Pb isotopic composition of sulfides and Lu-Hf isotope of zircons in the Tuolangla deposit are given in Supplementary Tables S2 and S3, respectively.

4. Result

4.1. Zircon U-Pb ages

The U-Pb ages of zircons separated from the three

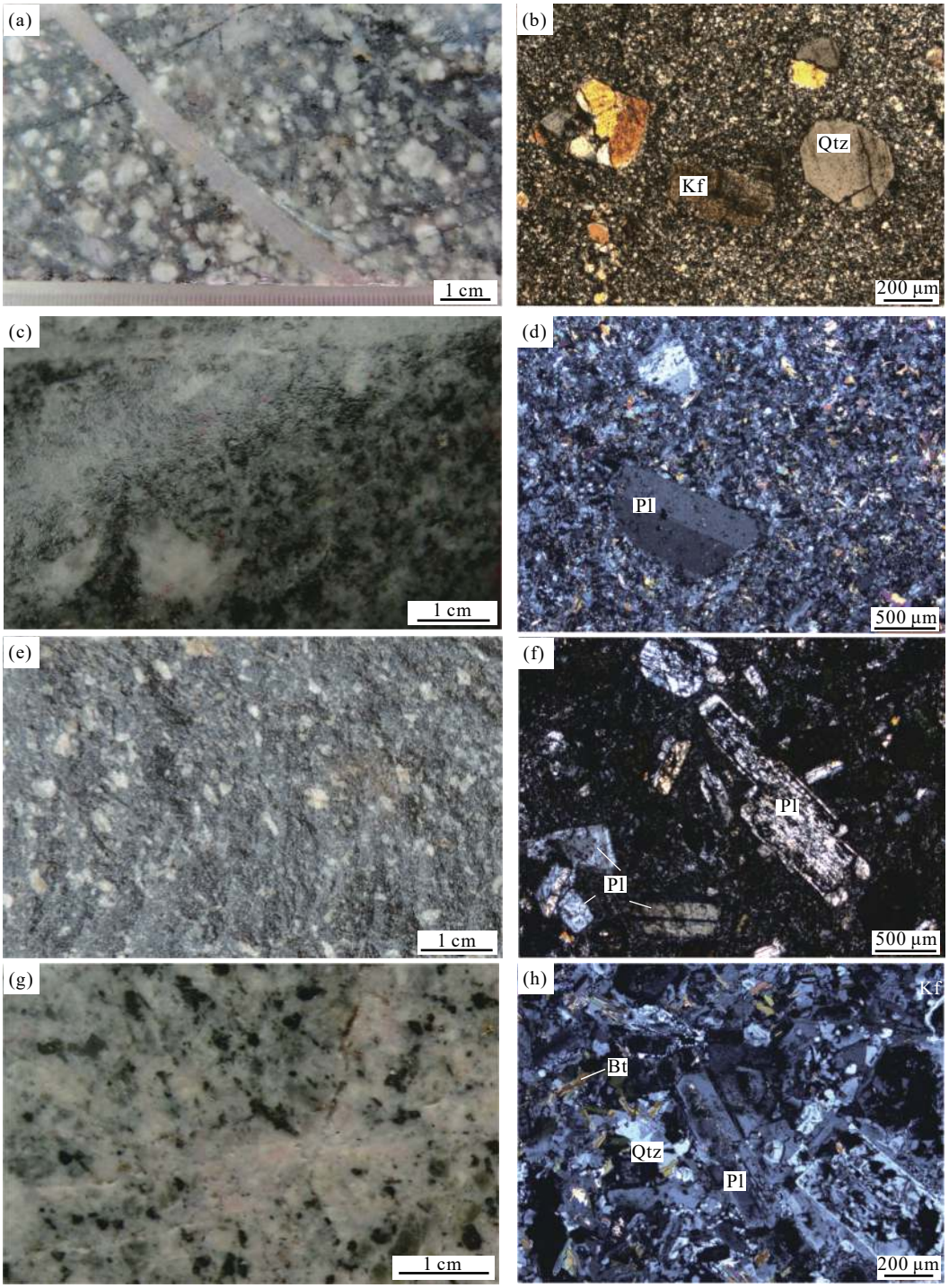

Fig. 2. Photographs and micrographs of intrusive rocks in Tuolangla deposit. a–b sample photographs and micrographs of the granite porphyry; c–d sample photographs and micrographs of the biotite granodiorite; e–f sample photographs and micrographs of the hornblende diorite; g–h sample photographs and micrographs of the granodiorite porphyry. Pl–Plagioclase, Qtz–Quartz, Bt–Biotite, Kf–K-feldspar.

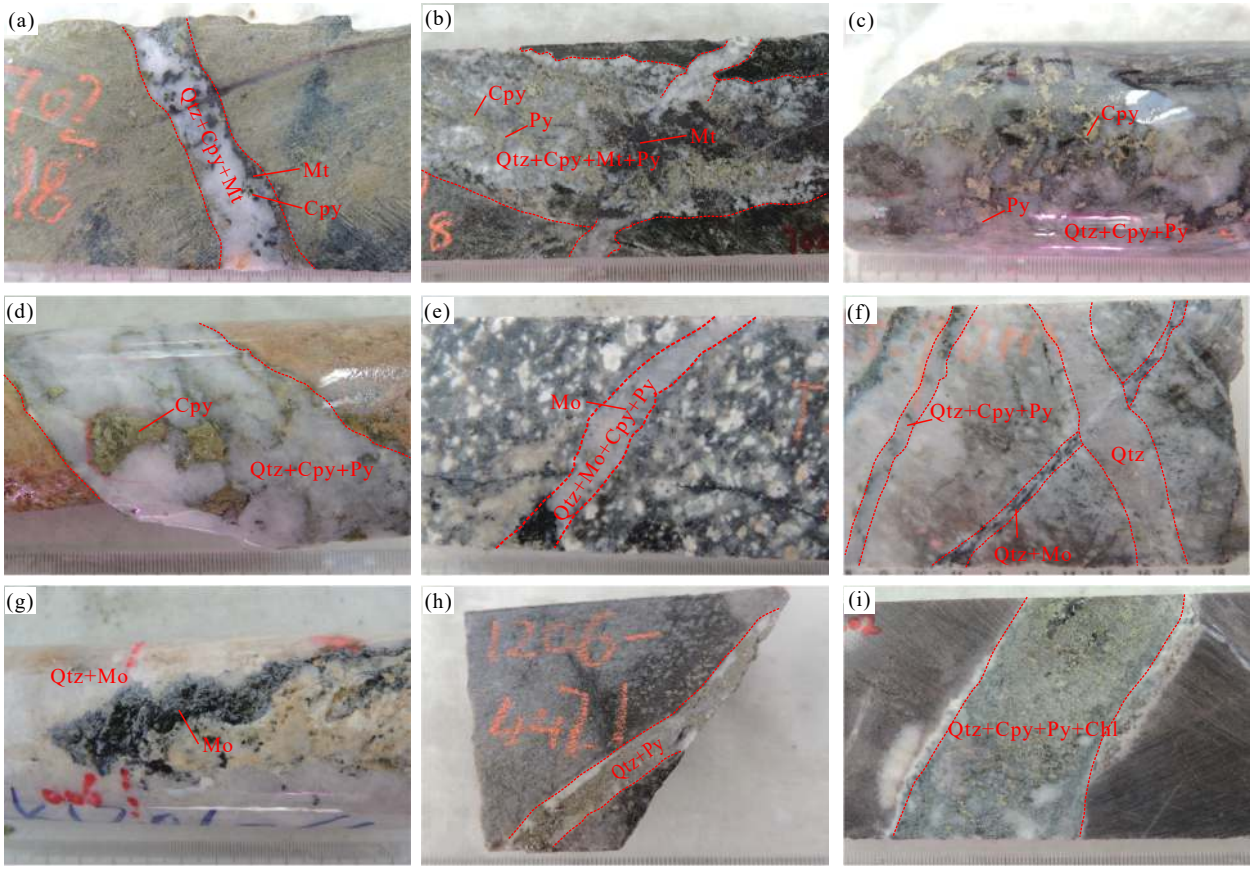

Fig. 3. Hand specimen of drill-core samples showing different vein types. a–Qtz+Cpy+Mt vein; b–Qtz+Cpy+Mt+Py vein cut by barren white quartz vein; c and d–Qtz+Cpy+Py vein with strong silicification; e–Qtz+Mo+Cpy+Py vein with sericitic alteration envelope; f–Qtz+Mo veinlet cut by barren white Qtz vein; g–Qtz+Mo vein. h–Py+Qtz vein; i–Qtz+Cpy+Py+Chl vein with sericite alteration envelope. Qtz–Quartz, Cpy–Chalcopyrite, Py–Pyrite, Mo–Molybdenite, Mt–Magnetite, Chl–Chlorite.

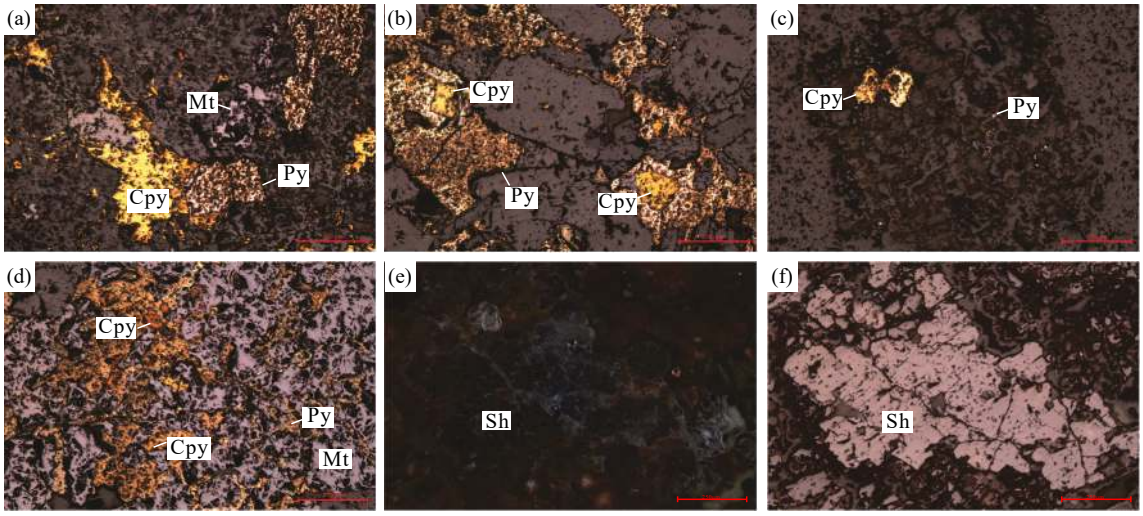

Fig. 4. Microphotographs of drill-core samples showing the mineralization paragenetic relationship at the Tuolangla deposit. Py–Pyrite, Cpy–Chalcopyrite; Mt–Magmatite; Sh–Scheelite.

samples are listed in Table 1. Most grains are transparent and colorless to light brown and show obvious oscillatory zoning. Zircons from the granite porphyry (Sample 1201) are euhedral to subhedral, about 100–200 μm long and length-to-width ratios from 2∶1 to 3∶1. Zircons from the hornblende diorite (Sample TL15-9) are subhedral and 130–220 μm long with length-to-width ratios from 1∶1 to 3∶1. Zircons from the granodiorite porphyry (Sample TL15-8) are prismatic to euhedral and about 100–230 μm long with length-to-width ratios from 1∶1 to 3∶1.

The U-Pb ages of zircons are plotted in Fig. 5. Eighteen grains from the granite porphyry (Sample 1201) have

Table 1. LA-ICP-MS zircon U−Pb ages of the rocks in the Tuolangla deposit

No.	Content		Th/U	Isotopic ratios				Ages/Ma				Concordance
	$Th/10^{-6}$	$U/10^{-6}$		$^{207}Pb/^{235}U$	±1σ	$^{206}Pb/^{238}U$	±1σ	$^{207}Pb/^{235}U$	±1σ	$^{206}Pb/^{238}U$	±1σ	
Sample 1201 granite porphyry, drillhole ZK 1201, depth: 144.5m												
1	141.49	381.90	0.37	0.11205	0.00773	0.01607	0.00019	107.8	7.06	102.8	1.21	95.4%
2	278.44	449.03	0.62	0.11230	0.00623	0.01600	0.00017	108.1	5.68	102.3	1.05	94.6%
3	521.13	883.88	0.59	0.09782	0.00727	0.01602	0.00020	94.8	6.73	102.4	1.24	92.0%
4	144.76	331.56	0.44	0.12175	0.02321	0.01600	0.00038	116.7	21.01	102.3	2.44	87.7%
5	132.93	351.63	0.38	0.12208	0.00807	0.01580	0.00021	117	7.3	101	1.32	86.3%
6	121.31	292.46	0.41	0.10611	0.01040	0.01585	0.00022	102.4	9.54	101.4	1.38	99.0%
7	168.52	466.96	0.36	0.10478	0.00802	0.01583	0.00022	101.2	7.37	101.3	1.37	99.9%
8	194.76	453.14	0.43	0.12431	0.00903	0.01621	0.00021	119	8.15	103.6	1.36	87.1%
9	163.16	379.33	0.43	0.09767	0.00811	0.01579	0.00020	94.6	7.5	101	1.29	93.2%
10	118.92	216.72	0.55	0.11096	0.01769	0.01595	0.00031	106.8	16.17	102	1.96	95.5%
11	384.50	870.89	0.44	0.12190	0.00451	0.01625	0.00015	116.8	4.08	103.9	0.94	90.0%
12	242.19	523.23	0.46	0.14265	0.00748	0.01582	0.00020	135.4	6.64	101.2	1.3	74.7%
13	150.76	379.35	0.40	0.10506	0.00736	0.01613	0.00019	101.4	6.76	103.2	1.18	98.2%
14	199.04	480.22	0.41	0.09683	0.00607	0.01597	0.00018	93.8	5.62	102.1	1.12	91.2%
15	147.02	468.54	0.31	0.11458	0.00594	0.01580	0.00018	110.1	5.41	101.1	1.13	91.8%
16	168.08	514.50	0.33	0.10508	0.00619	0.01564	0.00019	101.5	5.69	100	1.2	98.5%
17	680.37	927.69	0.73	0.10452	0.00565	0.01607	0.00018	100.9	5.19	102.8	1.16	98.1%
18	196.52	414.25	0.47	0.10197	0.00731	0.01589	0.00021	98.6	6.74	101.6	1.34	97.0%
Sample TL15-9 hornblende diorite												
1	200.97	214.19	1.13	0.06913	0.01525	0.00972	0.00034	67.9	14.5	62.3	2.2	91%
2	396.81	371.52	1.00	0.05920	0.00778	0.00993	0.00028	58.4	7.5	63.7	1.8	91%
3	314.55	307.31	1.04	0.05875	0.00669	0.00971	0.00025	58.0	6.4	62.3	1.6	92%
4	230.08	233.88	1.06	0.05888	0.00590	0.00981	0.00023	58.1	5.7	62.9	1.4	92%
5	558.98	498.16	0.96	0.06903	0.00731	0.00986	0.00036	67.8	6.9	63.2	2.3	93%
6	273.19	362.26	1.43	0.06938	0.00724	0.00993	0.00029	68.1	6.9	63.7	1.9	93%
7	214.45	252.29	1.27	0.06939	0.00979	0.00991	0.00028	68.1	9.3	63.6	1.8	93%
8	615.54	721.59	1.28	0.06064	0.00521	0.00989	0.00026	59.8	5.0	63.5	1.6	94%
9	194.24	280.48	1.58	0.06650	0.00653	0.00965	0.00035	65.4	6.2	61.9	2.2	94%
10	314.26	350.50	1.18	0.06822	0.00618	0.00999	0.00028	67.0	5.9	64.1	1.8	95%
11	413.75	424.06	1.06	0.06692	0.00411	0.00984	0.00015	65.8	3.9	63.1	1.0	95%
12	488.70	385.97	0.83	0.06652	0.00482	0.00976	0.00022	65.4	4.6	62.6	1.4	95%
13	441.32	496.45	1.21	0.06715	0.00665	0.00997	0.00027	66.0	6.3	63.9	1.7	96%
14	316.23	359.92	1.23	0.06691	0.00662	0.00990	0.00026	65.8	6.3	63.5	1.6	96%
15	183.15	244.22	1.40	0.06489	0.00699	0.00961	0.00022	63.8	6.7	61.6	1.4	96%
16	397.53	343.16	0.91	0.06285	0.00477	0.00986	0.00021	61.9	4.6	63.3	1.4	97%
17	405.64	478.05	1.27	0.06489	0.00977	0.00971	0.00022	63.8	9.3	62.3	1.4	97%
18	318.77	373.46	1.24	0.06333	0.00936	0.00991	0.00031	62.4	8.9	63.6	2.0	98%
19	667.00	688.95	1.11	0.06085	0.00430	0.00949	0.00025	60.0	4.1	60.9	1.6	98%
20	264.84	267.20	1.08	0.06489	0.00466	0.00982	0.00021	63.8	4.4	63.0	1.3	98%
21	129.54	177.43	1.49	0.06539	0.00584	0.00992	0.00023	64.3	5.6	63.6	1.5	98%
22	124.84	168.63	1.47	0.06600	0.00711	0.00998	0.00036	64.9	6.8	64.0	2.3	98%
23	601.99	582.64	1.06	0.06248	0.00679	0.00975	0.00026	61.5	6.5	62.6	1.6	98%
24	277.52	308.41	1.21	0.06551	0.00467	0.00993	0.00022	64.4	4.4	63.7	1.4	98%
25	461.20	462.70	1.07	0.06414	0.00633	0.00994	0.00029	63.1	6.0	63.8	1.8	99%
26	319.19	386.64	1.31	0.06396	0.00653	0.00989	0.00027	63.0	6.2	63.4	1.7	99%
27	159.37	184.55	1.21	0.06184	0.00512	0.00957	0.00025	60.9	4.9	61.4	1.6	99%
Sample TL15-8 granodiorite porphyry												
1	3415.45	1198.40	0.38	0.02241	0.00206	0.00343	0.00009	22.5	2.0	22.1	0.5	98%
2	204.46	150.85	0.80	0.02136	0.01210	0.00350	0.00032	21.5	12.0	22.5	2.1	95%
3	545.50	520.17	1.02	0.02330	0.00225	0.00351	0.00008	23.4	2.2	22.6	0.5	96%
4	150.82	1225.89	8.73	0.02320	0.00176	0.00355	0.00007	23.3	1.7	22.9	0.4	98%
5	793.87	320.89	0.45	0.02220	0.00249	0.00356	0.00010	22.3	2.5	22.9	0.6	97%
6	1453.50	2056.78	1.52	0.02363	0.00298	0.00364	0.00009	23.7	3.0	23.4	0.6	98%
7	521.28	357.52	0.74	0.02448	0.00419	0.00366	0.00010	24.6	4.2	23.6	0.7	95%

Table 1. (*Continued*)

No.	Content		Th/U	Isotopic ratios				Ages/Ma				Concordance
	$Th/10^{-6}$	$U/10^{-6}$		$^{207}Pb/^{235}U$	±1σ	$^{206}Pb/^{238}U$	±1σ	$^{207}Pb/^{235}U$	±1σ	$^{206}Pb/^{238}U$	±1σ	
8	1359.67	1186.08	0.94	0.02408	0.00298	0.00368	0.00009	24.2	3.0	23.7	0.6	98%
9	372.73	179.55	0.52	0.02484	0.00254	0.00370	0.00012	24.9	2.5	23.8	0.8	95%
10	1651.54	433.52	0.28	0.02552	0.00414	0.00382	0.00013	25.6	4.1	24.6	0.9	96%

Table 2. Re-Os isotopic analyses of molybdenite from the Oligocene Mo±W±Cu deposits in Gangdese metallogenic belt

Sample	m/g	Re/(μg/g)	2σ	Os/(ng/g)	2σ	^{187}Re/(μg/g)	2σ	^{187}Os/(ng/g)	2σ	Age/Ma	2σ	Reference
Nuri Cu-W-Mo deposit												
CB-63	0.00648	447.5	3.3	3.706	0.094	281.3	2.1	115.7	0.9	24.7	0.34	Zhang S et al., 2012
CB-65	0.00684	315.3	2.4	5.078	0.062	198.2	1.5	81.58	0.66	24.71	0.34	
CB-68	0.00538	395.6	3.4	0.1179	0.0299	248.6	2.1	102.6	0.8	24.77	0.36	
NR-41	0.00399	396	4	0.018	0.1212	248.9	2.5	99.04	1.29	23.88	0.44	
NR-39	0.00447	554.3	5.2	0.358	0.0721	348.4	3.3	136.2	1.4	23.46	0.38	
NR-40	0.00426	605.5	5.5	0.1454	0.0553	380.6	3.5	149.7	1.3	23.61	0.36	
NR-49	0.00418	416.5	3.4	3.955	0.065	261.8	2.2	103.4	0.9	23.71	0.35	
NR-50	0.00426	285	2.4	17.27	0.21	179.1	1.5	70.96	0.58	23.77	0.34	
ZK4501-217	0.00444	337.5	2.7	2.082	0.129	212.1	1.7	86.16	0.76	24.37	0.35	
Panan Mo deposit												Duan LF et al., 2014
cb-2	0.00526	269.5	2.3	0.0133	0.0299	169.4	1.5	89.85	0.85	31.83	0.48	
cb-6	0.00592	238.9	2	0.039	0.0405	150.1	1.2	78.42	0.71	31.34	0.46	
cb-9	0.00522	322.7	2.5	0.0138	0.0619	209.1	1.6	110.6	0.9	31.74	0.44	
cb-19	0.00568	243.3	1.9	0.0262	0.0277	152.9	1.2	80.91	0.71	31.75	0.45	
Chenba Mo-Cu deposit												Sun X et al., 2013
MZ011-172	0.01006	86.3	0.8	0.082	0.021	54.2	0.5	27.02	0.23	29.9	0.44	
MZ011-164	0.00046	129.9	1.1	0.049	0.166	81.6	0.7	41.33	0.51	30.38	0.51	
MZ004-320	0.01039	299.8	2.5	0.38	0.064	188.4	1.6	95.59	0.81	30.44	0.44	
MZ004-321	0.00242	713	6.5	1.936	0.044	448.1	4.1	224.4	1.9	30.04	0.44	
Jigongcun Mo deposit												Zhang et al., 2013
JGC1	0.0023	1691	29	0.046	0.3115	1063	18	395.3	2.5	22.32	0.46	
JGC2	0.00243	1514	16	0.1902	0.1506	951.5	9.8	353.3	2.7	22.29	0.36	
JGC3	0.00213	1496	19	0.1642	0.1202	940.1	11.9	352.1	2.6	22.48	0.4	
JGC4	0.00237	1512	20	0.2447	0.2032	950.2	12.3	361.1	2.3	22.81	0.4	
JGC5	0.00211	1410	18	0.1633	0.1739	886.1	11.2	331.4	3.1	22.45	0.42	
Tuolangla Cu-W-Mo deposit												This study
T01	0.00448	369.7	5.6	0.719	0.0792	232.3	3.5	92.39	0.62	23.86	0.46	
T02	0.00511	460.8	4.1	0.2926	0.0371	289.6	2.6	113.2	0.7	23.47	0.34	
T03	0.00485	413.4	3.4	0.2808	0.0676	259.8	2.2	100.9	0.6	23.31	0.33	
T04	0.00485	26.08	0.22	0.2446	0.0604	16.39	0.14	6.526	0.07	23.89	0.4	
T05	0.00476	403.1	3	0.2351	0.0375	253.3	1.9	98.6	0.65	23.36	0.33	
T06	0.00548	419.8	3.5	0.2376	0.0325	263.8	2.2	103.2	0.6	23.47	0.34	
Mingze Mo deposit												Yan XY et al., 2010
MRoI-1	0.00466	365.7	3	1.6414	0.0609	229.8	1.9	116.08	0.94	30.31	0.42	
MRoI-2	0.00295	388.2	3	1.4862	0.0535	244	1.9	122.52	0.98	30.13	0.42	
MRoI-3	0.00327	233.7	1.8	0.3949	0.0469	146.9	1.1	73.53	0.68	30.04	0.44	
MRoI-4	0.00375	317.5	2.4	1.1617	0.0426	199.5	1.5	100.58	0.81	30.25	0.41	
MRoI-5	0.00315	334.1	2.7	1.8664	0.0506	210	1.7	106.32	0.85	30.38	0.42	
MRoI-6	0.00353	328	2.7	1.3155	0.0444	206.1	1.7	104.41	0.93	30.39	0.45	
MRoI-7	0.00388	361.9	3.4	1.6162	0.023	227.5	2.1	114.75	1.01	30.27	0.46	
MRoI-8	0.00366	419.5	3.1	1.1888	0.0635	263.7	2	131.69	1.06	29.97	0.41	

216.72×10^{-6}–927.69×10^{-6} U and 118.92×10^{-6}–680.37×10^{-6} Th with Th/U ratios of 0.31 to 0.73 (Table S1). The concordances of spots 4, 5, 8, 12 are less than 90%. Except for these four spots, fourteen grains have a concordant U-Pb age of 102.0±0.6 Ma (MSWD=0.82). This age is interpreted as the crystallization age of the zircons (Fig. 5a). Twenty-seven spots were made on zircon grains from the hornblende diorite (Sample TL15-9), which have 177.43×10^{-6}–688.95×10^{-6} U and 124.84×10^{-6}–667.00×10^{-6} Th with Th/U ratios of 0.91 to 1.58. All spots have concordance greater than 90%

and yielded U–Pb age of 63.0±0.6 Ma (MSWD=0.27) (Fig. 5b). Ten grains of zircons from the granodiorite porphyry (Sample TL15-8) have 150.8×10^{-6}–2056.8×10^{-6} U and 150.8×10^{-6}–3415.5×10^{-6} Th with variable Th/U ratios of 0.3 to 8.7. The granodiorite porphyry yielded a concordant U-Pb age of 23.1±0.2 Ma (MSWD=0.37), which is considered to be the crystallization age of the granodiorite porphyry. The granodiorite porphyry presents a similar age as with the molybdenite Re-Os age, which further indicates that mineralization is related to this intrusion (Fig. 5c).

4.2. Major and trace elements

Whole rock major and trace element data for the representative samples are listed in Table S1. All analyzed samples are metaluminous rock (Fig. 6b). The positive relationship between SiO_2 and P_2O_5 indicate that they are all I-type granites (Fig. 6d). The granodiorite porphyry is high K calc-alkaline series (Fig. 6a) and has variable SiO_2 (68.78% to 69.85%), Al_2O_3 (15.78% to 16.22%), MgO (0.95% to 1.08%). The $Mg^{\#}$ values of the granodiorite porphyry are 48.4 to 52.1. The granodiorite porphyry has similar trace element character with the Miocene mineralized porphyries. These rocks are enriched in some high field strength elements (HFSEs; e.g., Th, U and Pb) and large ion lithophile elements (LILEs; e.g., Rb, Ba and Sr), and are depleted of Nb and Ta (Fig. 7a). The granodiorite porphyry is enriched in LREEs and depleted in HREEs, with no Eu anomaly. $(La/Yb)_N$ values range from 36.0 to 40.3, indicating stronger fractional crystallization (Fig. 7b). There are also low concentrations of Y and Yb ($Y=5.53\times10^{-6}$–6.3×10^{-6}, $Yb=0.56\times10^{-6}$–0.64×10^{-6}) and high concentrations of Sr ($Sr = 896\times10^{-6}$–913×10^{-6}), indicating an adakitic affinity as defined by Defant MJ and Drummond MS, 1990 (Fig. 6c).

4.3. Molybdenite Re-Os geochronology

All molybdenite is separated from hydrothermal veins. The molybdenite Re-Os isotope analysis results are listed in Table 2. The Re contents of six molybdenite samples range from 26.08 10^{-6} to 460.8×10^{-6}, with an average of 348.8×10^{-6}. The ^{187}Re contents range variably from 6.5×10^{-9} to 113.2×10^{-9}, with an average of 219.2×10^{-9}. The $^{187}Re/^{187}Os$ ratios have a small range of 2.51 to 2.57. A regression analysis using ISOPLOT software was performed to yield an optimal isochron based on the Re-Os experimental data (Ludwig KR, 2003). The model ages are distributed between 23.31 Ma and 23.89 Ma with average of 23.56 Ma, and the weighted mean of model ages is 23.5±0.3 Ma (MSWD=0.42)

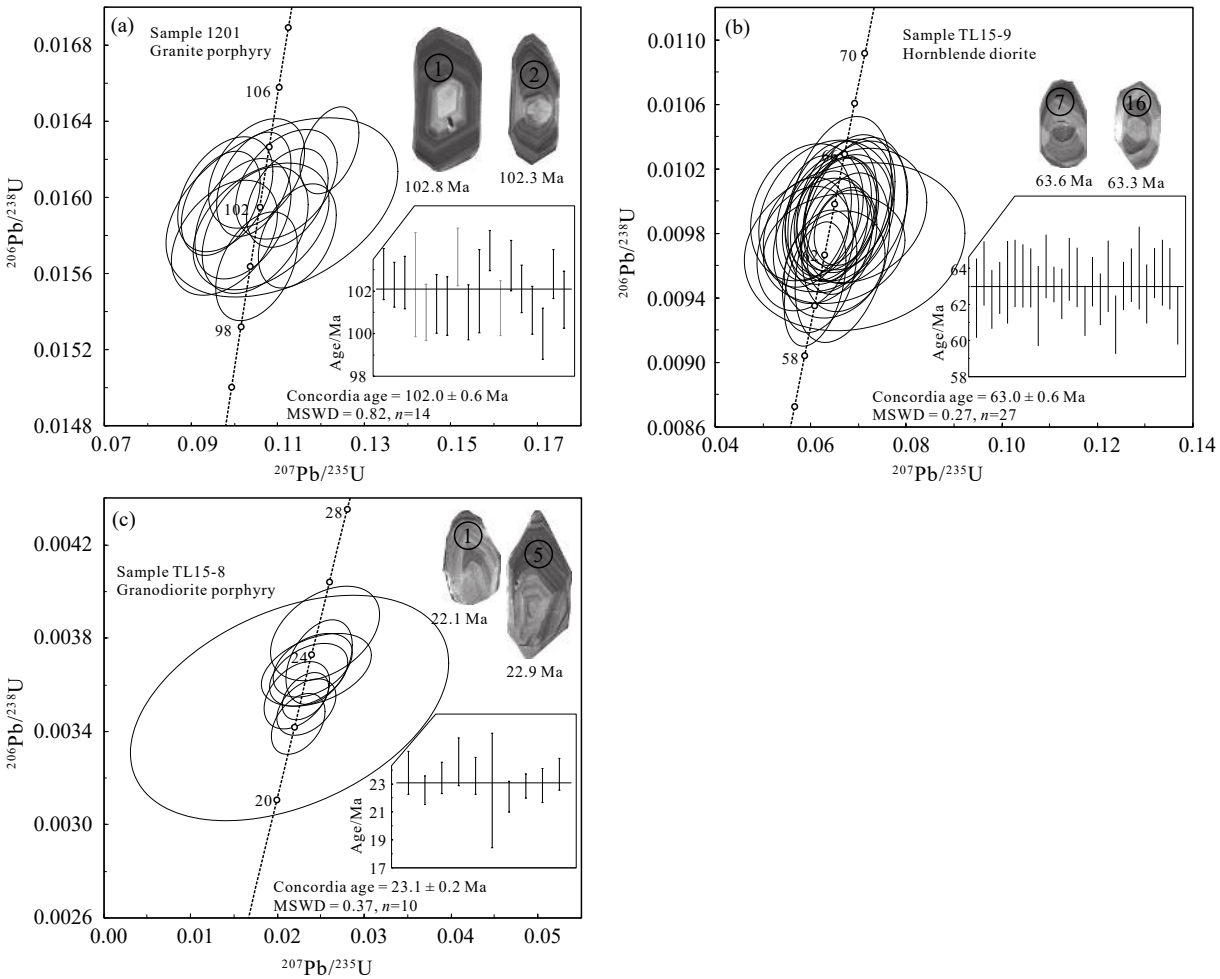

Fig. 5. Zircon U–Pb concordia diagrams ages of intrusive rocks.

(Fig. 8a), which represents the timing of mineralization.

4.4. S and Pb isotopic result

Lead and sulfur isotopic data of sulphides collected in this study are listed in Table S2. The published Pb isotopic data of other Cu-W-Mo and Cu-Mo deposits within this region are also plotted in Fig. 9. The lead isotope composition of the sulfides (pyrite and chalcopyrite) show little variation Pb isotope composition. Their $^{206}Pb/^{204}Pb$, $^{207}Pb/^{204}Pb$, and $^{208}Pb/^{204}Pb$ ratios range from 18.19 to 18.69, 15.57 to 15.67, and 38.24 to 38.80, respectively.

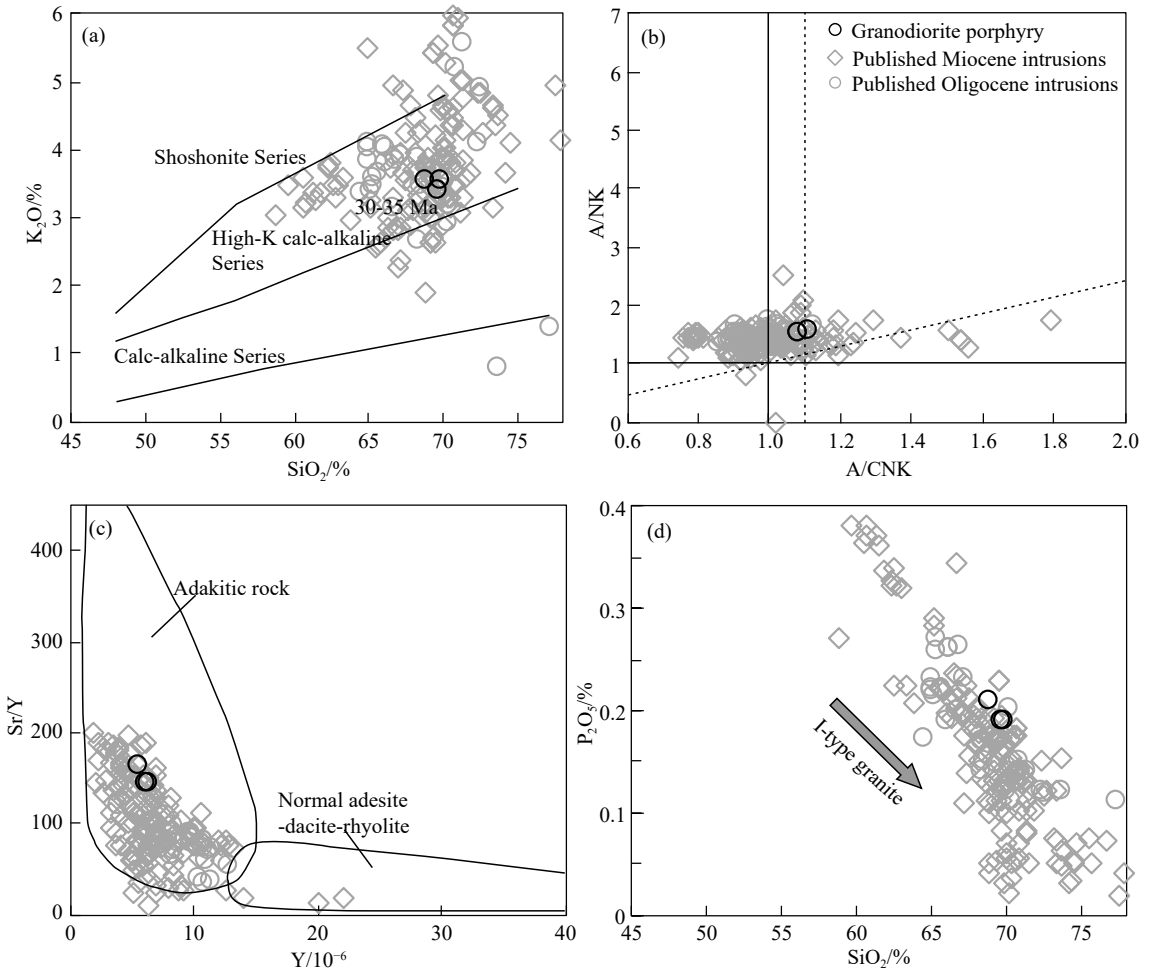

Fig. 6. Geochemistry plot diagram of granodiorite porphyry. a–SiO_2 *vs.* K_2O plot. b–A/NK vs. A/CNK diagram. c–Y *vs.* Sr/Y diagram (after Defant MJ and Drummond MS, 1990). d–SiO_2 *vs.* P_2O_5 plot. Published Oligocene and Miocene intrusive rocks in the Gangdese belt also plot in above figures, data from reference therein.

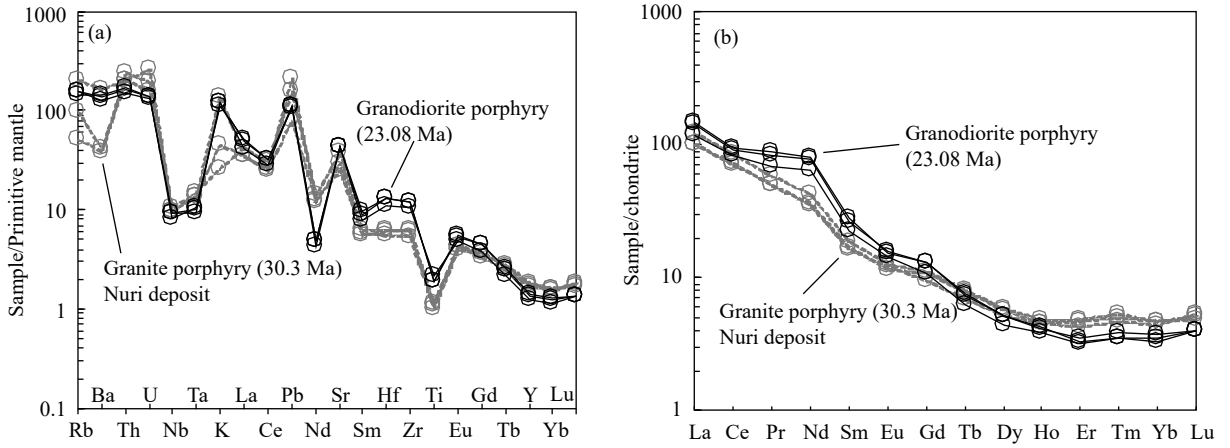

Fig. 7. Primitive mantle normalized multi-element patterns (a) and chondrite-normalized rare earth element (REE) patterns (b) of Tuolangla intrusive rocks. Chondrite and primitive mantle normalization values are from Sun and McDonough (1989).

Sulfides, including pyrite and chalcopyrite, exhibit relatively homogeneous isotopic compositions with $\delta^{34}S$ values range from 0.6‰ to 3.4‰ with an average of 2.2‰. Seven chalcopyrite samples have $\delta^{34}S$ values between 1.5‰ to 3.4‰, with average of 2.3‰. Six pyrite samples have $\delta^{34}S$ values between 0.6‰ to 3.3‰, with average of 2.1‰ (Fig. 10).

4.5. Lu-Hf isotopic composition

Zircon Lu-Hf dating is listed in Appendix Table S3. Ten zircons from the granodiorite porphyry for U-Pb dating were also analyzed for Hf isotopes (Table S3 and Fig. 11). The results show that the granodiorite porphyry has an initial $^{176}Hf/^{177}Hf$ ratio of 0.2830 to 0.2833 and $^{176}Lu/^{177}Hf$ ratio ranging from 0.0007 to 0.0024, with average at 0.2831 and 0.0012, respectively. The data suggests that the zircons have low radiogenic Hf concentration which indicates the measured $^{176}Hf/^{177}Hf$ ratio represents the Hf isotope composition of the system during zircon crystallization. Zircons from the granodiorite porphyry have $\varepsilon_{Hf}(t)$ values ranging from 7.7 to 12.9 with average of 10.9. Calculated two-stage model ages (T_{DM2}) vary from 274 Ma to 609 Ma with an average of 404 Ma, indicating that the magma was sourced from the depleted mantle.

5. Discussion

5.1. Petrogenesis of Oligocene (23.1 Ma) ore-bearing granodiorite porphyry

The geochemical composition of the granodiorite porphyry displays high SiO_2 (68.78%−69.75%) and K_2O (3.40%−3.56%) content, and belongs to high K calc-alkaline series (Fig. 6a). Their A/CNK values (1.08−1.11) are consistent with metaluminous to peraluminous characteristics, which are similar to the Miocene Cu-Mo related porphyries. The scatter distribution of P_2O_5 with increasing SiO_2 shows I-type characters (Fig. 6d). They are also enriched in LREE and LILE and are depleted in HFSE (such as Nb, Ta, Ti), and display high Sr and low Y and Yb content, and high Sr/Y (144−165), which plot within the adakite fields (Figs. 6c, 7),

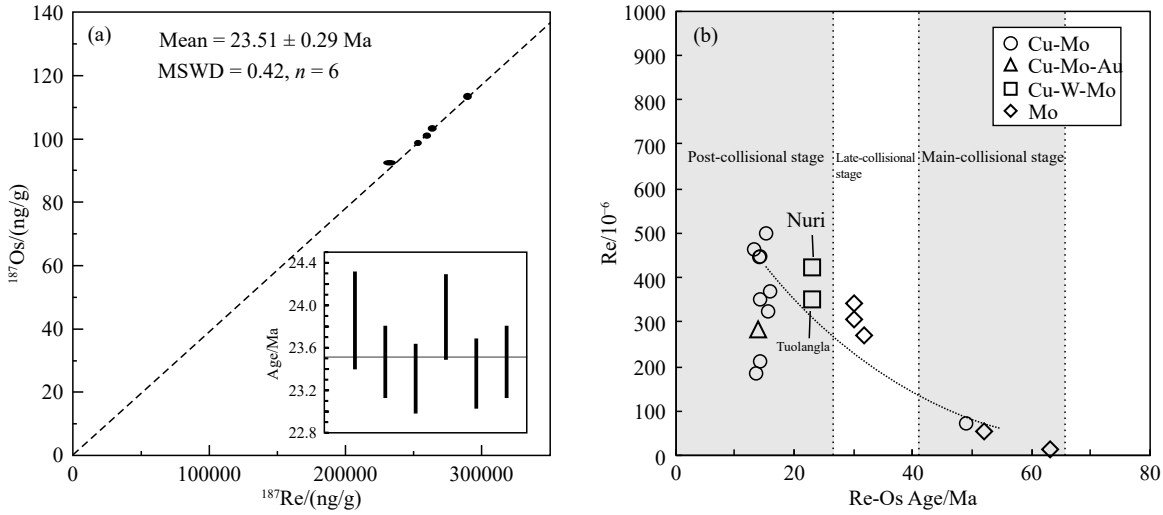

Fig. 8. Molybdenite Re-Os age of the Tuolangla deposit (a) and Re content of porphyry deposits in Gangdese belt (b).

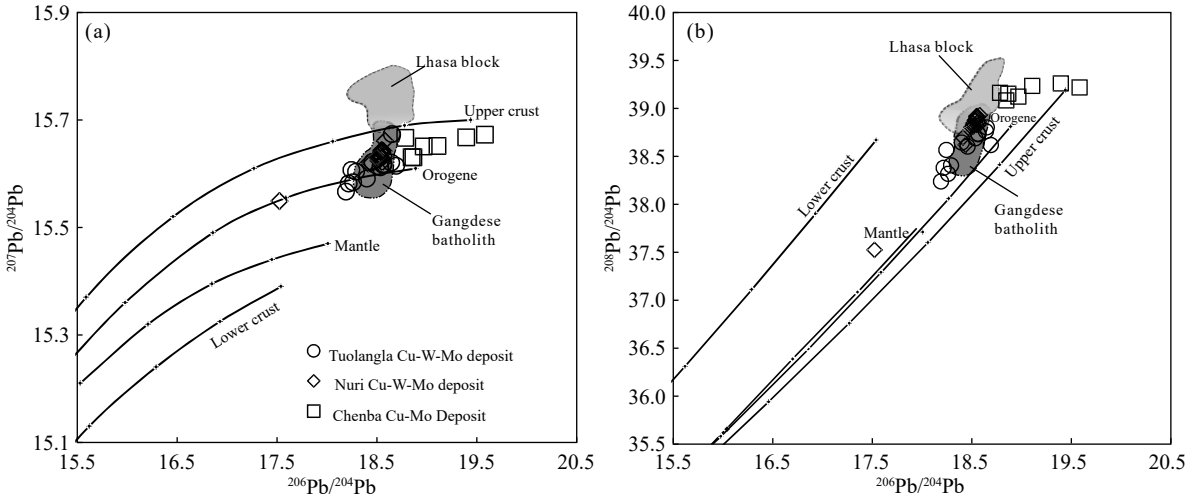

Fig. 9. Plumbotectonic diagrams of the ore sulphides in the Tuolangla deposit (after Stacey JS and Kramers JD, 1975; Zartman RE and Doe BR, 1981). Data of Nuri and Chenba from Wang LQ et al. (2014). Lhasa block and Gangdese batholith data from Gariépy C et al. (1985) and are also plotted in the diagram for comparison.

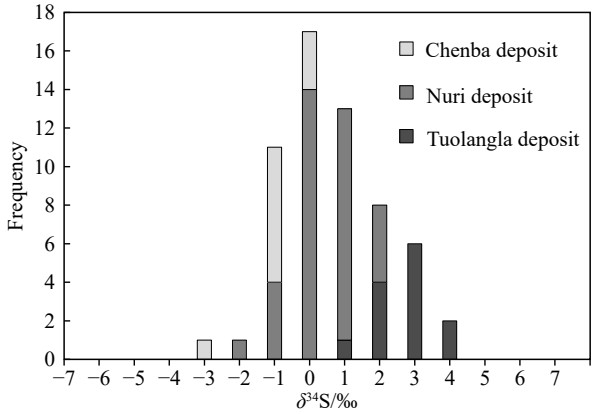

Fig. 10. Frequency distribution diagram of $\delta^{34}S$ values.

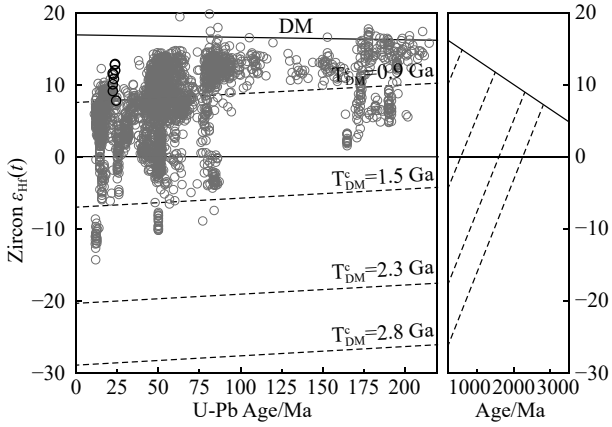

Fig. 11. Result of zircon Hf isotope concentrations for granodiorite porphyry from Tuolangla. Published zircon Hf isotope data also plotted on the diagram for reference.

which is similar to the Miocene adakite-like rocks of magmatism belt of southern Tibet. Four models have been proposed for the generation of the non-arc setting Gangdese adakites, including: (1) Partial melting of the subducted Neotethyan oceanic crust, followed by interaction with the overlying mantle wedge (Qu XM et al., 2007); (2) partial melting of a thickened of continental crust, or a newly formed mafic lower crust (Hou ZQ et al., 2011, 2013; Li JX et al., 2011); (3) partial melting of an upper mantle source metasomatized by slab-derived melts (Gao Y et al., 2007); and (4) partial melting of the subducted Indian continental crust beneath the southern Lhasa terrane (Xu WC et al., 2010).

The collision of the Indian and Asian plates and the break-off of Neo-Tethys oceanic slab from the Indian lithospheric mantle occurred prior 50 Ma (Chung SL et al., 2005, 2009; Ji WQ et al., 2009). Therefore, the Oligocene granodiorite porphyry cannot have formed by the melting of subducted oceanic crust. The geochemical composition of the granodiorite porphyry shows relatively low MgO (0.95% to 1.08%), Cr (2.4×10^{-6} to 4.09×10^{-6}), Ni (2.79×10^{-6} to 3.58×10^{-6}), Sr (896×10^{-6} to 913×10^{-6}) contents, and $Mg^{\#}$ (48.4 to 52.1) values when compared to low-SiO_2 and high $Mg^{\#}$ adakites that come directly from the mantle, which suggests that the granodiorite porphyry is not a mantle-derived adakite. Also, there is no contemporaneity mafic stock exposed in southern Tibet and therefore a metasomatized upper mantle is not a suitable source for the granodiorite porphyry. Other Oligocene and Miocene potassic and ultrapotassic rocks from southern Gangdese, which exhibit high MgO, and high MgO/Na_2O ratio, and low $\varepsilon_{Hf(t)}$ values (less than −6.3), are interpreted to be formed by partial melting of the subduction of the Indian plate beneath the Lhasa terrane (Tian SH et al., 2017). The granodiorite porphyry shows very positive $\varepsilon_{Hf(t)}$ values (7.7 to 12.9) (Table S3) close to values from the depleted mantle (Fig. 12) which also rule out the possibility that the porphyry magmas were derived directly from the subducted Indian continental crust beneath the southern Lhasa terrane. The granodiorite porphyry exhibits similar geochemical composition to the Miocene ore-bearing porphyries. This means that the granodiorite porphyry has a similar magma resource as the Miocene ore-bearing porphyries.

All magmatic zircons in the granodiorite porphyry give a relatively young Hf model ages (T_{DM}^{c}: 274–608 Ma) and very positive $\varepsilon_{Hf}(t)$ values (7.7−12.9), which overlap with values of T_{DM}^{C} and $\varepsilon_{Hf(t)}$ for zircons in the Miocene adakite-like porphyries (Fig. 10). These granitoids have been regarded as being derived from a juvenile curst under the Gangdese orogenic belt (Hou ZQ et al., 2011; Hou ZQ et al., 2013; Hou ZQ et al., 2015). Relatively young T_{DM}^{C} ages indicate that the source for the granodiorite porphyry magma was a juvenile mafic lower-crust (Fig. 12).

5.2. Sources of ore-forming materials

Lead and sulfur isotopes of sulphides have been proven to be one of the most effective tools to establish the source of the ore-forming materials. This study obtained the S and Pb isotopes of ore sulfides from the Tuolangla deposit to constrain its source (Tang JX et al., 2015; Zhou JX et al., 2018a, 2018b; Luo K et al., 2019).

As shown in Fig. 9, most of the Pb isotopic data plot on the orogen evolution line, which are similar to the Nuri deposit. Pyrite and chalcopyrite show a wide range of variation in $^{206}Pb/^{204}Pb$ (18.19−18.69) and also a smaller range in $^{207}Pb/^{204}Pb$ (15.57−15.67). The heterogeneities in

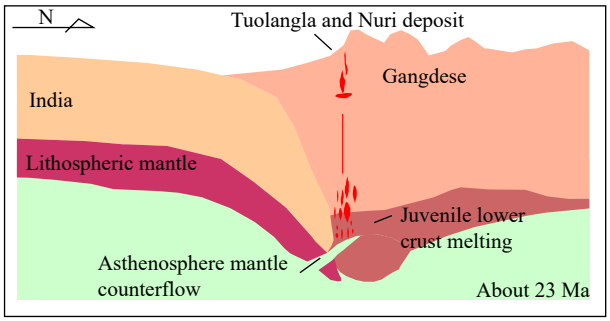

Fig. 12. Cartoon model for Oligocene evolution of southern Tibet. Part melting of juvenile lower curst involved of ancient materials (about 23 Ma).

$^{207}Pb/^{204}Pb$ are the same magnitude as the Gangdese batholith, ranging from 15.59 to 15.74 (Gariépy C et al., 1985) (Fig. 9a), and have more radiogenic $^{207}Pb/^{204}Pb$ than the Indian Ocean MORB. This Pb isotopic composition pattern reflects a mixture of Pb derived from the mantle and ancient crust. This interpretation is consistent with previously published data (Wang LQ et al., 2014) and, with this model; all samples appear to contain crustal Pb.

Sulfates are absent in the Tuolangla deposit, therefore the $\delta^{34}S$ average value of the sulfides are approximately equal to that of the hydrothermal fluids. $\delta^{34}S$ values of the ore sulfides in the Tuolangla deposit vary from 0.6‰ to 3.4‰ with an average of 2.2‰ and, when plotted in a histogram, show a tower distribution (Fig. 10), indicating the type of magma source.

The Re content of molybdenite is an effective tool to trace ore-forming materials. The Re contents in molybdenite increase in magnitude from crust through to mantle sourced deposits (Mao JW et al., 1999). The Tuolangla deposit shows extremely variable Re content in the molybdenite (26.08×10^{-6}–460×10^{-6}). Generally, molybdenite derived from crust have Re contents that are tens of $\times10^{-6}$ to below 1×10^{-6} level in contrast with those of mantle, which have a much higher Re content (e.g., hundreds to tens of hundreds) (Mao JW et al., 1999). Therefore, the Re content in molybdenite at the Tuolangla deposit reflects a mixture of Re derived from the mantle and crust (Fig. 8b).

5.3. Implication for regional metallogeny

The mineralization age of the Tuolangla deposit has been constrained by molybdenite Re-Os dates of the quartz-sulfide veins, which formed during the main mineralization. The molybdenites, even though they have variable Re values (Table 2), have yielded a limited range of Re-Os ages (23.31–23.89 Ma), which is identical to previously reported Re-Os ages for the Nuri deposit (23.46−24.77 Ma) (Zhang S et al., 2012), and the Gangqiongla deposit (22.29–22.81 Ma) (un-published). Our study demonstrates that the U-Pb and molybdenite Re-Os dates obtained for the timing of crystallization of the granodiorite porphyry and associated Cu-W-Mo mineralization are in excellent agreement. Thus, minor disseminated Mo mineralization and quartz-sulfide veins are also present in the granodiorite porphyry and skarn mineralization is present at the contact of the intrusion. This indicates that the stock is associated with the Cu-W-Mo mineralization during the post-collision stage of India-Eurasia collision. Recent drilling shows that the porphyry-type Cu-W-Mo mineralization is present in the Nuri deposit (Zheng YY et al., 2015), which indicates that the porphyry system could exists at the south sub-belt of the GPCB. Previous studies argued that there are three metallogenic epochs for Mesozoic magmatism which lead to the formation of the porphyry-skarn deposits within the GPCB, occurring at ca. 63–49 Ma, 31–30 Ma, 23–13 Ma (Ying LJ et al., 2010; Meng XJ et al., 2003; 2009; Zeng YC et al., 2015; Zhang S et al., 2012; Duan LF et al., 2014) (Fig. 8b). These are consistent with collisional processes within the Tibetan orogeny, including: (1) Main-collisional convergent setting (about 65−41 Ma); (2) late-collisional transform structural setting (about 40−26 Ma); and (3) post-collisional crustal extension setting (about 25−0 Ma) (Hou ZQ et al., 2009) (Fig. 8b). The main-collisional metaollognesis took place in a convergent setting. Metallogenesis during this period formed porphyry Mo and Cu-Mo deposits, e.g., Sharang, Jiru. The late-collisional metallognesis occurred mainly in a transform structural setting and is characterized by Cenozoic strike-slip fault, shearing, and thrust systems. Metallogenesis during this period mainly formed porphyry Mo deposits, e.g., Mengze, Chenba, Panan. The post-collisional metallogenesis occurred in a crustal extensional setting dominated by lithospheric mantle delamination, crustal shortening and synchronal extension at shallower crustal levels. Metallogenesis during this period formed porphyry Cu-Mo deposits, porphyry Cu-Mo-Au deposits, and porphyry-skarn Cu-W-Mo deposits, e.g., Qulong, Jiama, Zhunuo, Tinggong, Bairong, Nuri, and Tuolangla (Fig. 8b).

According to Hou ZQ (2015), the formation of giant Miocene PCDs within the GPCB were formed by the re-melting of the juvenile lower crustal sulfide-bearing Cu-rich Jurassic cumulates, which was triggered by Cenozoic crustal thickening and/or underplating of earlier asthenospheric melts. Compared with Miocene Cu-Mo mineralization in GPCB, the Oligocene mineralization in south margin of the Gangdese metallogenic belt has a different composition, although the causes of the different mineralization associations are not clear. The results of our study allow us to shed light on the distinctions between the Oligocene and Miocene metallogenic stocks.

The Zedang terrane was once considered to be an intra-oceanic arc during the Cretaceous. This terrane is in contact with ophiolitic rocks to its south and continental margin arc volcanics and intrusions of the Gangdese batholith and other rocks of the Lhasa terrane to its north (Aitchison JC et al., 2000). The authors propose that the Oligocene porphyry skarn Cu-W-Mo mineralization is associated with the previous terrane. This finding may clarify why the Oligocene deposits are found only in the Zedang area and why mineralization types and degree of the Oligocene mineralization are considerably different from those of the Miocene mineralization.

6. Conclusions

(i) The Tuolangla deposit is a newly discovered porphyry-skarn Cu-W-Mo deposit within the south GPCB.

(ii) The granitoid plutons in the Tuolangla region are composed of granite porphyry, hornblende diorite, and granodiorite porphyry. Zircon U-Pb ages of these plutons yield ages of 102.1 Ma, 63.0 Ma, and 23.1 Ma, respectively.

(iii) The Re-Os weighted mean age of 23.5 ± 0.3 Ma was obtained from molybdenite and coincides with the emplacement of the ore-bearing porphyries, which display the similar whole-rock geochemistry and zircon Lu-Hf isotopic

composition with Miocene mineralization porphyries indicating that the source for the granodiorite porphyry magmas was also likely a juvenile mafic lower-crust.

(iv) The authors proposed that the Oligocene porphyry skarn Cu-W-Mo mineralization is probably associated with the previous Zedang terrane. This finding may clarify why the Oligocene deposits are found only in the Zedang area and why mineralization types of the Oligocene mineralization are considerably different from those of the Miocene mineralization.

Acknowledgement

The authors thank the reviewers and the Editor-in-Chief for their constructive comments. This study is supported by the National Key Research and Development program of Ministry of Sciences and Technology (2018YFC0604103, 2016YFC0600308), Chinese Geological Survey Project (DD20190147) and China Scholarship Council (CSC). The authors thank the Science and Technology Innovation Team of the geology and prospecting of the Tibetan plateau for assistance during this study.

CRediT authorship contribution statement

Yong Huang conceived and planned the experiments. Yong Huang and Wei Liang carried out the experiment. Yong Huang wrote the manuscript with support from Ming-Hua Ren, Guang-ming Li, Kelly Heilbronn, Zuo-wen Dai and Yi-yun Wang. Guang-ming Li and Li Zhang helped supervise the project. Yong Huang conceived the original idea.

Declaration of competing interest

The authors declare no conflicts of interest.

Supplementary data

Supplementary data (Appendix A, Table S1, Table S2, and Table S3) to this article can be found online at doi: 10.31035/cg2020047.

References

Aitchison JC, Badengzhu, Davis AM, Liu JB, Luo H, Malpas JG, McDermid IRC, Wu HY, Ziabrev SV, Zhou MF. 2000. Remnants of a Cretaceous intra-oceanic subduction system within the Yarlung-Zangbo suture (southern Tibet). Earth and Planetary Science Letters, 183(1–2), 231–244.

Beaudoin G, Hébert R, Wang CS, Tang, J. 2005. Epithermal Au-Ag-Cu, porphyry Cu-(Au-Mo) and Cu-Au-Ag-Zn-Pb skarn deposits of the Gangdese Arc, Tibet. Mineral Deposit Research: Meeting the Global Challenge, Springer Berlin Heidelberg, 1219–1222.

Burg JP, Chen GM. 1984. Tectonics and structure zonation of southern Tibet, China. Nature, 311, 219–223. doi: 10.1038/311219a0.

Chen L, Qin KZ, Li GM, Li JX, Xiao B, Zhao JX, Fan X. 2015. Zircon U-Pb ages, geochemistry, and Sr-Nd-Pb-Hf isotopes of the Nuri intrusive rocks in the Gangdese area, southern Tibet: Constraints on timing, petrogenesis, and tectonic transformation. Lithos, 212–215, 379–396. doi: 10.1016/j.lithos.2014.11.014.

Chung SL, Chu MF, Ji J, O'Reilly SY, Pearson NJ, Liu D, Lee TY, Lo CH. 2009. The nature and timing of crustal thickening in Southern Tibet: Geochemical and zircon Hf isotopic constraints from postcollisional adakites. Tectonophysics, 477(1–2), 36–48.

Chung SL, Chu MF, Zhang Y, Xie Y, Lo CH, Lee TY, Lan CY, Li X, Zhang Q, Wang Y. 2005. Tibetan tectonic evolution inferred from spatial and temporal variations in post-collisional magmatism. Earth-Science Reviews, 68(3), 173–196.

Defant MJ, Drummond MS. 1990. Derivation of some modern arc magmas by melting of young subducted lithosphere. Nature, 347(6294), 662–665. doi: 10.1038/347662a0.

Duan LF, Li W, Zheng YC, Liang W, Fu Q, Li QY. 2014. Post-collisional Oligocene metallogenic process in southern margin of Gandise belt: Evidence from Re-Os dating of molybdenite from the Panan porphyry Mo deposit. Acta petrologica ET Mineralogica, 33(2), 307–316 (in Chinese with English abstract).

Gao Y, Hou Z, Kamber BS, Wei R, Meng X, Zhao R. 2007. Lamproitic rocks from a continental collision zone: Evidence for recycling of subducted Tethyan oceanic sediments in the mantle beneath Southern Tibet. Journal of Petrology, 48(4), 729–752. doi: 10.1093/petrology/egl080.

Gariépy C, Allègre CJ, Xu RH. 1985. The Pb-isotope geochemistry of granitoids from the Himalaya-Tibet collision zone: Implications for crustal evolution. Earth and Planetary Science Letters, 74(2), 220–234.

Hou ZQ, Gao YF, Qu XM, Rui ZY, Mo XX. 2004. Origin of adakitic intrusives gener-ated during mid-Miocene east–west extension in southern Tibet. Earth and Planetary Science Letters, 220, 139–155. doi: 10.1016/S0012-821X(04)00007-X.

Hou ZQ, Yang ZS, Qu XM, Meng XJ, Li ZQ, Beaudoin G, Rui ZY, Gao YF, Zaw K. 2009a. The Miocene Gangdese porphyry copper belt generated during post-collisional extension in the Tibetan Orogen. Ore Geology Reviews, 36(1–3), 25–51.

Hou ZQ, Cook NJ. 2009b. Metallogenesis of the Tibetan collisional orogen: A review and introduction to the special issue. Ore Geology Reviews, 36(1–3), 2–24. doi: 10.1016/j.oregeorev.2009.05.001.

Hou ZQ, Zhang HR, Pan XF, Yang ZM. 2011. Porphyry Cu (-Mo-Au) deposits related to melting of thickened mafic lower crust: Examples from the eastern Tethyan metallogenic domain. Ore Geology Reviews, 39(1–2), 21–45. doi: 10.1016/j.oregeorev.2010.09.002.

Hou ZQ, Zheng YC, Yang ZM, Yang ZS. 2012. Metallogenesis of continental collision setting: Part Ⅰ. Gangdese Cenozonic porphyry Cu-Mo systems in Tibet. Mineral Deposits, 31(4), 647–670 (in Chinese with English abstract).

Hou ZQ, Zhen YC, Yang ZM, Rui ZY, Zhao ZD, Jiang SH, Qu XM, Sun QZ. 2013. Contribution of mantle components within juvenile lower-crust to collisional zone porphyry Cu systems in Tibet. Mineralium Deposita, 48(2), 173–192. doi: 10.1007/s00126-012-0415-6.

Hou ZQ, Yang ZM, Lu YJ, Kemp A, Zheng YC, Li QY, Tang JX, Yang ZS, Duan LF. 2015. A genetic linkage between subduction- and collision-related porphyry Cu deposits in continental collision zones. Geology, 43(3), 247–250. doi: 10.1130/G36362.1.

Hou ZQ, Zhou Y, Wang R, Zeng YC, He WY, Zhao M, Noreen JE, Roberto FW. 2017. Recycling of metal-fertilized lower continental crust: Origin of non-arc Au-rich porphyry deposits at cratonic edges. Geology, 45(6), 563–566. doi: 10.1130/G38619.1.

Huang Y, Li GM, Ding J, Dai J, Yan GQ, Dong SL, Huang HX. 2017. Origin of the newly discovered Zhunuo porphyry Cu-Mo-Au deposit in the western part of the Gangdese porphyry copper belt in the southern tibetan plateau, SW China. Acta Geologica Sinica (English Edition), 91(1), 109–134. doi: 10.1111/1755-6724.13066.

Huang Y, Tang JX, Ding J, Zhang L, Lang XH. 2013. The Re-Os isotope system of the Xiongcun porphyry copper-gold deposit, Tibet. Geology in China, 40(1), 302–311 (in Chinese with English

abstract).

Ji WQ, Wu FY, Chung SL, Li JX, Liu CZ. 2009. Zircon U-Pb geochronology and Hf isotopic constraints on petrogenesis of the Gangdese batholith, southern Tibet. Chemical Geology, 262(3–4), 229–245.

Jiang ZQ, Wang Q, Wyman DA, Tang GJ, Jia XH, Yang YH, Yu HX. 2011. Origin of ~30 Ma Chongmuda adakitic intrusive rocks in the southern Gangdese region, south-ern Tibet: Partial melting of the northward subducted Indian continent crust? Geochimica, 40, 126–146 (in Chinese with English abstract).

Lee HY, Chung SL, Lo CH, Ji J, Lee TY, Qian ZQ. 2009. Eocene Neotethyan slab breakoff in southern Tibet inferred from the Linzizong volcanic record. Tectonophysics, 477(1–2), 20–35.

Li GM, Liu B, Qu WJ, Lin FC, She HQ, Feng CY. 2005. The Porphyry-Skarn ore- Forming system in Gangdese Metallogenic belt, southern Xizang: Evidence from molybdenite Re-Os Age of Porphyry-type copper deposits and Skarn-type copper polymetallic deposits. Geotectonica ET Metallogenic, 29(4), 482–490 (in Chinese with English abstract).

Li GM, Qin KZ, Ding KS, Liu TB, Li JX, Wang SH, Jiang SY, Zhang XC. 2006. Geology, Ar-Ar age and mineral assemblage of Eocene skarn Cu-Au±Mo deposits in the Southeastern Gangdese Arc, Southern Tibet: Implications for deep exploration. Resource Geology, 56(3), 315–336. doi: 10.1111/j.1751-3928.2006.tb00286.x.

Li JX, Qin KZ, Li GM, Xiao B, Chen L, Zhao JX. 2011. Post-collisional ore-bearing adakitic porphyries from Gangdese porphyry copper belt, southern Tibet: Melting of thickened juvenile arc lower crust. Lithos, 126(3–4), 265–277.

Luo K, Zhou JX, Huang ZL, Wang XC, Wilde SA, Zhou W, Tian L. 2019. New insights into the origin of early Cambrian carbonate-hosted Pb-Zn deposits in South China: A case study of the Maliping Pb-Zn deposit. Gondwana Research, 70, 88–103. doi: 10.1016/j.gr.2018.12.015.

Ludwig KR. 2003. User's manual for Isoplot 3.00: A geochronological toolkit for Microsoft Excel. Berkeley Geochronology Center Special Publication, (4), 71.

Mao JW, Zhang Z, Zhang Z, Du AD. 1999. Re-Os isotopic dating of molybdenites in the Xiaoliugou W (Mo) deposit in the northern Qilian mountains and its geological significance. Geochimica et Cosmochimica Acta, 63(11–12), 1815–1818.

Meng XJ, Hou ZQ, Gao YF, Huang W, Qu XM, Qu WJ. 2003. Re-Os dating for molybdenite from Qulong porphyry copper deposit in Gangdese metallogenic belt, Xizang and its metallogenic significance. Geological Review, 49(6), 660–666 (in Chinese with English abstract).

Meng YK, Xu ZQ, Xu Y, Ma SW. 2018. Late triassic granites from the Quxu Batholith shedding a new light on the evolution of the Gangdese Belt in Southern Tibet. Acta Geologica Sinica (English Edition), 92(2), 462–481. doi: 10.1111/1755-6724.13537.

Miller C, Schuster R, Klötzli U, Frank W, Purtscheller F. 1999. Post-collisional potassic and ultrapotassic magmatism in SW Tibet: Geochemical and Sr-Nd-Pb-O isotopic constraints for mantle source characteristics and petrogenesis. Journal of Petrology, 40(9), 1399–1424. doi: 10.1093/petroj/40.9.1399.

Mo XX, Hou ZQ, Niu YL, Dong GC, Qu XM, Zhao, ZD, Yang ZM. 2007. Mantle contributions to crustal thickening during continental collision: Evidence from Cenozoic igneous rocks in southern Tibet. Lithos, 96, 225–242. doi: 10.1016/j.lithos.2006.10.005.

Mo XX, Niu YL, Dong GC, Zhao ZD, Hou ZQ, Zhou S, Ke S. 2008. Contribution of syncollisional felsic magmatism to continental crust growth: A case study of the Paleogene Linzizong volcanic Succession in southern Tibet. Chemical Geology, 250(1–4), 49–67.

Pan GT, Mo XX, Hou ZQ, Zhu DC, Wang LQ, Li GM, Zhao ZD, Gen QR, Liao ZL. 2006. Spatial-temporal framework of the Gangdese Orogenic belt and its evolution. Acta Petrologica Sinica, 22(3), 521–533 (in Chinese with English abstract).

Qu XM, Hou ZQ, Zaw K, Li YG. 2007. Characteristics and genesis of Gangdese porphyry copper deposits in the southern Tibetan Plateau: Preliminary geochemical and geochronological results. Ore Geology Reviews, 31(1–4), 205–223.

Rui ZY, Hou ZQ, Qu XM, Wang LQ, Wang LS, Liu YL. 2003. Metallogenetic epoch of gangdese porphyry copper belt and uplift of Qianghai-Tibet plateau. Mineral Deposits, 22(3), 217–225 (in Chinese with English abstract).

Sillitoe RH. 2010. Porphyry copper systems. Economic Geology, 105, 3–41. doi: 10.2113/gsecongeo.105.1.3.

Stacey JS, Kramers JD. 1975. Approximation of terrestrial lead isotope evolution by a two stage model. Earth and Planetary Science Letters, 26, 207–221. doi: 10.1016/0012-821X(75)90088-6.

Sun SS, McDonough WF. 1989. Chemical and isotopic systematics of oceanic basalts: implications for mantle composition and processes. Geological Society, 42, 313–345. doi: 10.1144/GSL.SP.1989.042.01.19.

Sun X, Zheng YY, Wu S, You ZM, Wu X, Li M, Zhou TC, Dong J. 2013. Mineralization age and petrogenesis of associated intrusions in the Mingze-Chengba porphyry-skarn Mo-Cu deposit, Gangdese. Acta Petrologica Sinica, 29(4), 1392–1406 (in Chinese with English abstract).

Sun X, Zheng YY, Xu J, Huang LH, Guo F, Gao SB. 2017. Metallogenesis and ore controls of Cenozoic porphyry Mo deposits in the Gangdese belt of southern Tibet. Ore Geology Reviews, 81, Part 2, 996–1014.

Tafti R, Lang JR, Mortensen JK, Oliver JL, Rebagliati CM. 2014. Geology and geochronology of the Xietongmen (Xiongcun) Cu-Au porphyry district, Southern Tibet, China. Economic Geology, 109(7), 1967–2001. doi: 10.2113/econgeo.109.7.1967.

Tafti R, Mortensen JK, Lang JR, Rebagliati M, Oliver JL. 2009. Jurassic U-Pb and Re-Os ages for the newly discovered Xietongmen Cu-Au porphyry district, Tibet, PRC: Implications for metallogenic epochs in the southern Gangdese belt. Economic Geology, 104(1), 127–136. doi: 10.2113/gsecongeo.104.1.127.

Tang JX, Lang XH, Xie FW, Gao YM, Li ZJ, Huang Y, Ding F, Yang HH, Zhang L, Wang Q, Zhou Y. 2015. Geological characteristics and genesis of the Jurassic No. I porphyry Cu-Au deposit in the Xiongcun district, Gangdese porphyry copper belt, Tibet. Ore Geology Reviews, 70, 438–456. doi: 10.1016/j.oregeorev.2015.02.008.

Tang Y, Qin YD, Gong XD, Duan YY, Chen G, Yao HY, Liao JX, Liao SY, Wang DB, Wang BD. 2020. Discovery of eclogites in Jinsha River suture zone, Gonjo County, eastern Tibet and its restriction on Paleo-Tethyan evolution. China Geology, 3, 83–103. doi: 10.31035/cg2020003.

Tian SH, Yang ZS, Hou ZQ, Mo XX, Hu WJ, Zhao Y, Zhao XY. 2017. Subduction of the Indian lower crust beneath southern Tibet revealed by the post-collisional potassic and ultrapotassic rocks in SW Tibet. Gondwana Research, 41, 29–50. doi: 10.1016/j.gr.2015.09.005.

Turner S, Arnaud N, Liu J, Rogers N, Hawkesworth G, Harris N, Kelley S, Van CP, Deng W. 1996. Post-collision, shoshonitic volcanism on the Tibetan Plateau: Implications for convective thinning of the lithosphere and the source of ocean island basalts. Journal of petrology, 37(1), 45–72. doi: 10.1093/petrology/37.1.45.

Wang LL, Mo XX, Li B, Dong GC, Zhao ZD. 2006. Geochronology and geochemistry of the ore-bearing porphyry in Qulong Cu(Mo) ore deposit, Tibet. Acta Petrologica Sinica, 22(4), 1001–1008 (in Chinese with English abstract).

Wang LQ, Tang JX, Chen W, Luo MC, Jiang HZ, Zhang K. 2014. Sulfur and Lead isotopic geochemistry of the Nuri and Chengba Cu-Mo-W depoisits in Tibet. Acta Geoscientica Sinica, 35(1), 39–48 (in

Chinese with English abstract).

Wang YY, Zeng LS, Gao LE, Gao JH, Hu ZP, Wang HT, Li GX, Di YL, Shen Y, Xu Q. 2020. Baddeleyite and zircon U-Pb ages of the ultramafic rocks in Chigu Tso area, Southeastern Tibet and their constraints on the timing of Comei Large Igneous Province. China Geology, 3(2), 262–268. doi: 10.31035/cg2020017.

Wu CD, Zheng YC, Zhang S, Fu Q, Xu PY. 2015. Ar-Ar Age of Biotite from the Nuri Cu-W-Mo deposit in Tibet, and Its geodynamic significance. Acta Geologica Sinica, 89(9), 1673–1682 (in Chinese with English abstract).

Xu WC, Zhang HF, Guo L, Yuan HL. 2010. Miocene high Sr/Y magmatism, south Tibet: Product of partial melting of subducted Indian continental crust and its tectonic implication. Lithos, 114(3–4), 293–306.

Yan XY, Huang SF, Du AD. 2010. Re-Os ages of large Tungsten, Copper and Molybdenum deposit in the Zetang orefield, Gangdise and Marginal strike-slip transforming metallogenesis. Acta Geologica Sinica, 84(3), 398–406 (in Chinese with English abstract).

Yang YF, Mao JW, Chen YJ, Sun WD, Ni P, Yang XY. 2019. Hydrothermal ore deposits in collisional orogens. Science Bulletin, 64, 205–212. doi: 10.1016/j.scib.2019.01.007.

Yang ZM, Hou ZQ, Whit NC, Chang ZS, Li ZQ, Song YC. 2009. Geology of the post-collisional porphyry copper –molybdenum deposit at Qulong, Tibet. Ore Geology Reviews, 36(1–3), 133–159.

Yang ZM, Goldfarb R, Chang ZS. 2016. Generation of Postcollisional Porphyry Copper Deposits in Southern Tibet Triggered by Subduction of the Indian Continental Plate[A]//in JP Richards (eds.), Tectonics and Metallogeny of the Tethyan Orogenic Belt, Special Publication No. 19, the Society of Economic Geologists, 392.

Yin A, Dubey CS, Webb AAG, Kelty TK, Grove M, Gehrels GE, Burgess WP. 2010. Geologic correlation of the Himalayan orogen and Indian craton: Part 1. Structural geology, U-Pb zircon geochronology, and tectonic evolution of the Shillong Plateau and its neighboring regions in NE India. Geological Society of America Bulletin, 122(3–4), 336–359.

Yin A, Harrison TM. 2000. Geologic evolution of the Himalayan-Tibetan orogen. Annual Review of Earth and Planetary Sciences, 28(1), 211–280. doi: 10.1146/annurev.earth.28.1.211.

Ying LJ, Wang DH, Tang JX, Chang ZS, Qu WJ, Zheng WB, Wang H. 2010. Re-Os dating of Molybdenite from the Jiama polymetallic deposit in Tibet and its metallogenic significance. Acta Geologica Sinica, 84(8), 1165–1174 (in Chinese with English abstract).

Ying LJ, Wang CH, Tang JX, Wang DH, Qu WJ, Li C. 2014. Re-Os systematics of sulfides (chalcopyrite, bornite, pyrite and pyrrhotite) from the Jiama Cu-Mo deposit of Tibet, China. Journal of Asian Earth Sciences, 79, 497–506. doi: 10.1016/j.jseaes.2013.10.004.

Zartman RE, Doe BR. 1981. Plumbotectonics —the model. Tectonophysics, 75, 135–162. doi: 10.1016/0040-1951(81)90213-4.

Zeng YC, Chen JL, Xu JF, Lei M, Xiong QW. 2015. Origin of Miocene Cu-bearing porphyries in the Zhunuo region of the southern Lhasa subterrane: Constraints from geochronology and geochemistry. Gondwana Research, 41, 51–64.

Zhang S, Zheng YC, Huang KQ, Li W, Sun QZ, Li QY, Fu Q, Liang W. 2012. Re-Os dating of molybdenite from Nuri Cu-W-Mo deposit and its geological significance. Mineral Deposits, 31(2), 337–346 (in Chinese with English abstract).

Zhang SK, Zheng YY, Zhang GY, Gao SB, Sun X, Yu M, Guo JW, Xu Z. 2013. Geochronological constraints on Jigongcun quartz-vein type molybdenum deposit in Quxu County, Tibet. Mineral Deposits, 32(3), 641–648.

Zhao JX, Qin KZ, Li GM, Cao MJ, Evans NJ, McInnes BIA, Li JX, Xiao B, Chen L. 2015. The exhumation history of collision-related mineralizing systems in Tibet: Insights from thermal studies of the Sharang and Yaguila deposits, central Lhasa. Ore Geology Reviews, 65, 1043–1061. doi: 10.1016/j.oregeorev.2014.09.026.

Zhao JX, Qin KZ, Li GM, Li JX, Xiao B, Chen L, Yang YH, Li C, Liu YS. 2014. Collision-related genesis of the Sharang porphyry molybdenum deposit, Tibet: Evidence from zircon U-Pb ages, Re-Os ages and Lu-Hf isotopes. Ore Geology Reviews, 56, 312–326. doi: 10.1016/j.oregeorev.2013.06.005.

Zheng YY, Xiang S, Gao S.B, Wu S, Xu J, Jiang JS, Chen X, Zhao ZY, Liu Y. 2015. Metallogenesis and the minerogenetic series in the Gangdese polymetallic copper belt. Journal of Asian Earth Sciences, 103, 23–39. doi: 10.1016/j.jseaes.2014.11.036.

Zhou JX, Wang XC, Wilde SA, Luo K, Huang ZL, Wu T, Jin ZG. 2018a. New insights into the metallogeny of MVT Pb-Zn deposits: A case study from the Nayongzhi in South China, using field data, fluid compositions, and in situ S-Pb isotopes. American Mineralogist, 103, 91–108. doi: 10.2138/am-2018-6238.

Zhou JX, Xiang ZZ, Zhou MF, Feng YX, Luo K, Huang ZL, Wu T. 2018b. The giant Upper Yangtze Pb-Zn province in SW China: Reviews, new advances and a new genetic model. Journal of Asian Earth Sciences, 154, 280–315. doi: 10.1016/j.jseaes.2017.12.032.

Zhou S, Mo XX, Dong GC, Zhao ZD, Qiu RZ, Guo TY, Wang LL. 2004. ^{40}Ar-^{39}Ar geochronology of Cenozoic Linzizong volcanic rocks from Linzhou Basin, Tibet, China, and their geological implications. Chinese Science Bulletin, 49(18), 1970–1979. doi: 10.1007/BF03184291.

Zhu DC, Zhao ZD, Niu Y, Mo XX, Chung SL, Hou ZQ, Wang LQ, Wu FY. 2011. The Lhasa Terrane: Record of a microcontinent and its histories of drift and growth. Earth and Planetary Science Letters, 301(1–2), 241–255.